# PORTABLE HIGH-RESOLUTION AUTOMATED 3D IMAGING FOR FOOTWEAR AND TIRE IMPRESSION CAPTURE

by

**Yi-Hong Liao**

**A Thesis**

*Submitted to the Faculty of Purdue University*

*In Partial Fulfillment of the Requirements for the degree of*

**Master of Science**


Mechanical Engineering

West Lafayette, Indiana

December 2020

# THE PURDUE UNIVERSITY GRADUATE SCHOOL
# STATEMENT OF COMMITTEE APPROVAL

**Dr. Song Zhang, Chair**

School of Mechanical Engineering

**Dr. George Chiu**

School of Mechanical Engineering

**Dr. David Cappelleri**

School of Mechanical Engineering

**Approved by:**

Dr. Nicole Key

# ACKNOWLEDGMENTS

I would like to thank my family for supporting me on whatever I want to pursue throughout my entire life. I can not be grateful enough for their devotion and encouragement.

I want to thank my advisor Prof. Song Zhang for supporting me and giving me the opportunity to work with him. He always gives me guidance on research and cares about me whenever possible. When I am struggling with research, he encourages me and gives me positive advice. The excitement he always has on the research inspires me a lot. I am also very grateful to Prof. George Chiu, and Prof. David Cappelleri for serving on my advisory committee and taking their time to review my thesis and defense.

This research could not have been completed without all the works of many people. I would like to thank Prof. Tyler Bell for graphical user interface (GUI) software development, Prof. Song Zhang and Jae-Sang Hyun for developing the software and the hardware of the prototype systems, and other students in XYZTLab for their various contributions to this project at an early stage. Special thanks to forensic scientist Mr. James Wolfe for conducting high-quality lab tests, Mr. Ian Bortins and Mr. David Baldwin for the tire tread imaging experiment. Our team especially would like to express our gratitude to those who tested our prototype systems including Mr. William Henningsen and his team at the Omaha Police Department. In addition, we would like to thank those examiners and practitioners for providing valuable discussions and feedback at our workshops or presentations.

I would like to extend my gratitude to all of my colleagues in the lab past the present. They have provided me great help and friendship. Many thanks to Brian Acousta, Prof. Min Zhong, Xiaowei Hu, Prof. Andres Marrugo, Michael Crawford, George Gayton, Caroline Blanchard, Liming Chen, Kai-Chieh Chiang. In particular, I want to thank Michael Feller as he teaches me lots of things and gets me going on research when I joined the lab. He also introduces me the life at Purdue. Last but not least, I can not be thankful enough for Jae-Sang Hyun, who teach me everything in the lab when I first arrived at Purdue. I received immense help from him, and he is both a mentor and a friend for me as he gives advice not only in research but also in life.

I am also very thankful for all my friends who support and encourage me along the way on my research.

# TABLE OF CONTENTS

# LIST OF TABLES

# LIST OF FIGURES

# ABSTRACT

Footwear and tire impressions are critical evidence commonly found at a crime scene. However, they are often undervalued because they are hard to be captured and documented. Traditional 2D evidence quality photographs do not adequately provide metric depth information, and physical casts destroy the evidence afterward. Therefore, the forensic science community raised the need for improved evidence recognition, collection, and visualization analytical instrumentation for field and lab use. While the 3D optical techniques for imaging static objects have been extensively studied, there is still a major gap between current knowledge and collecting high-quality footwear and tire impressions evidence. Among optical means for 3D imaging, digital fringe projection (DFP) techniques reconstruct 3D shape from phase information, achieving camera-pixel spatial resolution. This paper presents a high-resolution 3D imaging technology using DFP techniques dedicated to footwear and tire impression capture. We developed fully automated software algorithms and a graphical user interface (GUI) that allow anyone without training to operate for high-quality 3D data capture. We performed accuracy evaluations and comparisons comparing with the commercial high-end 3D scanner and carried out qualitative tests for various impressions comparing with the current practices. Overall, our technology achieves similar levels of accuracy and resolution with a high-end commercially available 3D scanner, while having the merits of being 1) more affordable; 2) much easier to operate, and 3) more robust. Compared with the current practice of casting, our technology demonstrates its superiority because it 1) is non-destructive; 2) collects more evidence detail than casts, especially when an impression is fragile; 3) requires less time and money to collect each piece of evidence, and 4) results in a digital file that can easily be shared with other examiners.

# 1. INTRODUCTION

## 1.1 Motivation

Footwear and tire impressions are evidence often found at a crime scene. These impressions are distinct patterns made by treads of shoes or tires pressed or stamped on various substrates, such as soil, sand, snow, and even blood. The forensic examiners can identify the size, brand, and model of the shoe and tire from the patterns of their impressions. Because there are a wide variety of models of shoes and tires on the market with distinct patterns on their treads, identifying the model of the shoe or tire narrows down the group of suspects to a relatively small portion of the general public. Depending on the condition of the shoe and tire, each of them presents unique characteristics through wear and tear marks on the outsoles and tire surfaces. Therefore, just like fingerprints can lead to a specific individual, it is possible to match the specific impression to the exact shoe or tire that creates it. In addition, the examiners can obtain several clues relating to the criminal instance according to the footwear and tire impressions found at the crime scene. First, the number of suspects can be deduced according to the number of impressions found. Second, the approximate time the crime was committed can be determined from the condition and degeneration of the impressions made on fragile substrates. Third, the examiners can deduce the direction in which the suspect left the crime scene. These clues can be critical factors in solving criminal cases. Further, similar impressions found from different crime scenes can indicate that the crimes may be committed by the same suspect. For instance, a serial murderer has a high probability of leaving impressions of the same type of footwear at multiple crime scenes. More importantly, footwear and tire impressions can be combined with other types of forensic science evidence such as fingerprints, tool marks, and DNA which will provide strong evidence pointing toward the criminal [1].

Despite all the advantages mentioned above, footwear and tire impressions are often undervalued because of their ephemeral or transient nature. These impressions are easily altered, degenerated, and lost. Thus, it is always a challenging task for forensic examiners to capture and document this kind of evidence. Traditionally, impression evidence is documented by sketches, notes, electrostatic lifting, field forms, two-dimensional (2D) videos,

2D photographs, and physical casting. Two-dimensional evidence-quality photographs are commonly used to capture detailed features of the impressions. The proper techniques of capturing those photos involve placing a scale at the same depth and adjacent to the impression, aligning the camera image plane with the impression plane, adjusting the camera aperture to obtain the maximum depth of view, and illuminating the impression from various angles in order to minimize the shadowing and occlusion issue. It is hard for forensic photographers to apply these practices consistently every time [2]. In addition, more than one photograph with different illumination angles are usually needed to fully capture an impression. The quality of the photograph depends on the experience of the photographer and the type of camera used. Most importantly, 2D photographs do not adequately provide metric depth information. High-resolution three-dimensional (3D) information is critical for the accurate comparison between the imprints and the suspect's footwear and presumptive vehicle. Hence, 3D physical casting is often used as an effective supplement to these characteristics. Nonetheless, there are always several concerns regarding creating the physical cast of impressions. Proper casting techniques have to be conducted consistently and the correct casting material has to be chosen and produced. The biggest consideration of casting that should be taken into account is its invasive nature. The weight of the casting material risks destroying the evidence when pouring it into the impression. Furthermore, some impressions are in substrates that are resistant to conventional casting methods. Carrying out casting on an impression in sand is always problematic because sand is fragile and can easily collapse under the weight of the casting material. It is always a difficult assignment to recover impressions in snow because the temperature of the casting material will cause the snow to melt. In particular, when casting on wet snow, the casting material tends to flow with the melted snow [3].

In conclusion, the current method for shoe and tire impressions capture highly depends on the ability of the crime scene technicians' expertise to carry out their best practices in order to collect high-quality evidence. However, it is usually hard to consistently deliver such practices, even for the best technician. In addition to the fact that current methods require profound experience to perform, the conventional casting is destructive to the evidence. Hence, there is normally only one opportunity to capture the impression.

The Forensic Science Research and Development Technology Working Group (TWG) was tasked by the National Institute of Justice (NIJ) with identifying and prioritizing R&D to satisfy operational requirements for forensic science disciplines. In the field of Impression & Pattern/Trace Evidence, the TWG identified the operation needs in "Novel and/or improved evidence recognition, collection, and visualization tools and analytical instrumentation for field and lab use" [4]. In March 2016, The Organization of Scientific Area Committees for Forensic Science (OSAC) published a write up on the research need in the field of "Testing and Validation of 3D Imaging Technologies and associate products for Footwear and Tire Impressions Evidence". It states that the technology must be able to reproduce high-resolution tire/footwear impression evidence with sufficient detail and characteristic dimensions. Also, it should be affordable for law enforcement agencies, portable, and easy to use for examiners. The report assessed that "(there is a) major gap in current knowledge and no or limited current research is being conducted" [2].

Three-dimensional imaging devices that could capture details of impression evidence have been seen as an alternative and novel method that overcomes the drawbacks of current evidence recovery methods. Compared to casting, 3D imaging is non-invasive, thus will not harm the impression evidence. Forensic practitioners can capture the impression as many times as they want. Three-dimensional imaging techniques can be conducted relatively faster than casting. In addition, 3D imaging yields 3D digital files of the impression. These files can be put into commercially available 3D rendering software. Forensic practitioners can rotate and view the 3D model from various angles, adjust the lightings to ensure the details are not impeded by the shadows and numerous shaders can be applied onto the model to reveal any minute features of the impression. Another advantage is that, traditionally, with 2D photographs and physical casts of impressions, the comparison with the footwear, tires, or other impressions is done qualitatively. With the digital file, this can be conducted quantitatively. The physical casts are normally bulky, so the storage and retrieval of the physical cast is also a troublesome issue. On the contrary, hundreds of digital files can be store in just one small hard drive, and with the current cloud storage technology, these digital files can be easily uploaded onto the database against the need to compare them with any footwear or tire. Moreover, a digital file can be shared among forensic scientists

through email and clouds across the world in seconds. Last but not least, a digital file can be rendered into 2D images or be incorporated into animation footage that can be presented in the courtroom. When it is necessary, missing elements in impressions can be reconstructed as a reference by analyzing the 3D models created by 3D imaging devices. Those 3D models can also be fed into rapid prototyping to recreate the suspect's footwear and tires.

### 1.2 Literature review

Three-dimensional optical techniques for imaging static or quasi-static objects have been extensively studied over the past few decades, and have seen great success in medicine, virtual reality, and many other disciplines [5]. Optical methods to perform 3D imaging are typically based on triangulation (e.g., stereo vision, laser range scanning, space-time stereo, structured light). The main principle is that the imaging technique recovers depth (and therefore the three-dimensional structure of the object) by matching and geometrically relating distinct regions of a scene viewed from different angles. This is usually realized by analyzing two images with a digital image correlation (DIC) algorithm [6]. Three-dimensional optical techniques can be roughly separated into two categories: passive and active methods. In passive methods, there is no active illumination on the object. Instead, it depends on the light reflected from the measured object to reconstruct 3D. For example, stereo vision is a widely used 3D imaging method. Its principle is similar to how human eyes recover the depth of view. It utilizes two cameras to capture the object from different angles and then finds the correspondence between the pixels in the two images using the DIC algorithm. This approach is relatively simple since only two cameras are needed. It can achieve high-speed 3D reconstruction because a pair of images from two cameras are adequate for 3D recovery. Theoretically, the 3D reconstruction rate can be the same as the camera's frame rate. Nonetheless, the stereo vision comes with its own set of limitations. The calculation cost is high for executing the DIC algorithm, even if some studies try to lower the calculation effort by rectifying the images before it. Also, because the DIC approach relies upon the unique features of corresponding region pairs to perform matching, the measurement accuracy is low for surfaces with low texture variation such as a white plane.

Looking at a different method, active 3D optical techniques actively project random or known patterns onto the object to be measured. Because the system already has the information of the pattern, active methods can easily find the correspondence between images, often reaching higher resolution and accuracy than passive methods. Speckle technology [7] is a subset of stereo vision with various configurations. One configuration is a diffused laser light source or infrared emitter projecting random speckle patterns onto the measuring surface, another is to paint the scene with random patterns [8]. Then, the DIC algorithm is applied to recover the depth. Therefore, it resolves the problem in the standard stereo vision of low accuracy on surfaces lacking high texture variation, and such systems can achieve high temporal resolution (kHz or better). However, the fundamental problem of all stereo vision systems is that it is difficult for a stereo DIC method to attain camera-pixel spatial resolution because the DIC algorithm must match regions larger than one camera pixel. Furthermore, surface treatment (e.g., painting) often causes surface distortion which is not desirable.

Laser-range 3D scanning technologies actively project laser spots or lines onto the objects; as a result, they can be used to measure surfaces without strong texture variations. By analyzing the captured images, the 3D shape can be recovered through the triangulation of those laser spots or lines. Commercial laser scanners have been adapted to capture footwear and impression marks. For example, Bennett et al. [9] utilized a Konica-Minolta VI 900 laser scanner to measure footwear and impressions in soils. To demonstrate the difference in quality between conventional casting and laser scanning, both the impression and the physical cast are laser scanned and registered in Rapidform. The result shows that casting will create an area with a pouring artifact and laser scanning has greater precision and accuracy. In terms of time, conducting a 3D laser scanning is much faster than casting. However, the laser scanning system is quite bulky and has a high capital cost. The system's accuracy and resolution are rather low for capturing details of the impression. It resolves features to an accuracy of $\pm 0.1$ mm and achieved spatial resolution ( $\pm 0.22$ mm along x and $\pm 0.16$ mm along y, or 58 dpi along x and 79 dpi along y). It is also vulnerable under bright sunlight since VI 900 is designed for use in the laboratory, and the red laser light it uses can be affected by the ambient light levels. Prof. Tuceryan's research team [10]–[12] has developed an improved portable laser range scanning system for tire track impression

capture by employing two laser lights. The scanner stitches the two laser scans obtained from two laser lights at different angles, thus reducing the occlusion problem. Because the camera and laser are mounted on a linear railing system, they can move along the rail for at least 1.75 meters. Thus, this system is suitable for measuring impression evidence that spans a long spatial distance, such as a long tire track. The system also captures color texture images, but the resolution of the texture image along the scan direction depends on the speed that the camera moves. Knowing it takes approximately 20 minutes for the device to scan a 1.75m long surface, and the camera is capturing at 30fps, more than 36000 frames will be captured. For high-resolution images, this will take up several Gigabytes of storage. Along with this, its spatial resolution is quite low (0.2369mm along the direction perpendicular to the scanning motion). Furthermore, the system is still bulky and requires nontrivial on-site calibration. Komar, Davy-Jow, and Decker [13] also try to capture impression evidence with Polhemus FastSCAN Scorpion two laser hand-held unit (Colchester, VT). However, the unit and the necessary software cost $18000 USD in 2009. The system fails to image very faint sharp force kerf defects on human rib bones because of the size and limited visibility of the objects. Highly reflective surfaces can also interfere with the scan. Higher resolution 3D laser scanners have been used in other applications. Siderits et al [14], use a 3D laser scanner (NextEngine, Santa Monica California) to scan "crime scene gum". The indentation on the gum is used to reconstruct the tooth surface contour. The system costs less than $3000 USD and can achieve 0.127mm resolution. In general, the laser range scanning techniques are not ideal for high-spatial-resolution applications because the laser line is usually fairly wide.

Structured-light technologies increase the measurement capability by actively projecting known structured patterns onto the objects, performing the whole area measurement at once [15]. Numerous structured light techniques have been developed. Geng classifies all techniques into two categories: multi-shot and single-shot [5]. When the measuring object is static and the measuring time is not strictly constrained, multi-shot structure light techniques usually provide higher resolution and accuracy results. Although these techniques have been able to achieve time response in the tens of Hz [16]–[19], their spatial resolution is typically limited to being larger than a single projector's pixel as well as a single camera's pixel. Even though there are quite a number of commercial products on the market, such as the Microsoft

Kinect V1 and, Intel Realsense R200 and iPhone X, the forensic science community has not employed such a technique for impression mark capture to our knowledge. This is likely because it is difficult for these commercial systems to achieve the desired spatial resolution.

Fringe analysis is a special subset of structured light techniques that uses sinusoidal structured patterns to retrieve the 3D shape from carried phase information, rather than from the intensity information. This characteristic gives fringe analysis the benefit of immunity to the ambient light because it is canceled out between the sinusoidal structured patterns. Since these patterns have intensities that vary continuously from point to point in a known manner, they can boost the structured light techniques from projector-pixel resolution to camera-pixel resolution [20]. Because of the arctangent function in the phase retrieval process, the phase calculated from the sinusoidal patterns is wrapped in the interval $[-\pi, \pi]$, which has a $2\pi$ discontinuity between each period. Therefore, a phase unwrapping algorithm is needed to remove the $2\pi$ discontinuities. Phase unwrapping algorithms can be classified into spatial phase unwrapping and temporal phase unwrapping methods. Spatial phase unwrapping utilizes the phase information of the surrounding pixels in the same phase map to detect $2\pi$ discontinuities. However, it is very challenging for spatial phase unwrapping if the measuring surface has complex or sharp changing geometry [21]. On the other hand, temporal phase unwrapping eliminates $2\pi$ discontinuities by capturing additional images. Several temporal phase unwrapping algorithms have been developed. Some examples include the multi-frequency phase-shifting algorithms, simple coding method, and gray coding method. Fringe analysis techniques have been used extensively in high-precision 3D imaging using coherent light (laser) [22] or white-light interference [23] to generate sinusoidal patterns. Though laser and interference systems have high accuracy in micro scales, they typically require precise (e.g., tens of nanometers) mechanical adjustments (e.g., moving reference mirrors) to achieve phase shift, limiting their applications in macro-scale scanning. In this research, multi-step phase-shifting fringe analysis and the gray coding phase unwrapping method are used to retrieve phase information from the measuring surface geometry.

The digital fringe projection (DFP) technique uses digital video projectors instead of laser interference to generate sinusoidal patterns. This technique has the merits of lower cost, higher speed, and simplicity of development; thus, it has been a very active research area

within the past decade. Our team has developed systems to achieve 40 Hz [24] and 60 Hz [25] time response for 3D shape measurement acquisition. Recently, we have invented the binary defocusing technique [26] that allows us to use binary 1-bit patterns instead of 8-bit sinusoidal patterns, thus enhancing the capabilities of the DFP technique and achieved kHz [27] speeds. The accuracy, depth of view, and noise level can be adjusted by designing different binary patterns the projector projects. Generally, the more phase-shifted binary patterns are used, the lower the noise. Therefore, a combination of multi-step phase-shifting technique and the DFP technique is suitable for imaging static objects like footwear and tire impressions, since the object will not change during image acquisition. Because of the advantageous features of DFP methods, it was not a surprise to find that Buck et al. [3] had tried a DFP-based system (GOM ATOS II) to measure tire tracks in the snow and achieved probably the best spatial resolution (0.1 mm in both x and y) so far in this field; the same system has been used to digitally image ecstasy tablets, hemp coins, and imprint punches for forensic document examination purposes [28]. Thompson and Norris [29], also try to use structure light scanner PicoScan (4D Dynamics, Belgium) to capture footwear impression. The scanner demonstrates its capability to achieve 0.1 mm accuracy. The technical note also shows that it is easy to render or segment the digital model in commercially available software packages like CloudCompare (https://www.danielgm.net/cc/) or MeshLab (https://www.meshlab.net/). Further, it is possible to do a digital comparison between impressions and the footwear that creates them. On average, the users are able to scan the impression and complete any post-processes within 90 minutes. Yet, the guide for casting footwear and tire impression evidence from the Scientific Working Group for Shoeprint and Tire Tread Evidence (SWGTREAD) suggests that one should wait 48 hours for dental stone casts to thoroughly dry prior to any attempts to clean the cast [30].

Even though great improvements have been made toward achieving high speed, high resolution, and high accuracy, these technologies have mostly yet to leave the specialized laboratory environment. To our knowledge, there is not any inexpensive (<$10,000), portable, and fully automated high-resolution 3D optical imaging system.

## 1.3 Objective

This thesis presents a fully-automated 3D imaging system that allows the user to easily and quickly capture high-resolution footwear and tire impressions. The hardware was made to be portable and easy to set up; the software graphical user interface (GUI) was designed to be intuitive and thus users do not need training to operate it. Compared with the high-end commercially available 3D scanner (GOM ATOS Core, Germany, > US$30000), our technology achieves a similar level of accuracy and resolution, and our system has the merits of being 1) more affordable (a fractional cost of the commercial system); 2) much easier to operate; and 3) more robust. Compared with the current practice of casting, our technology demonstrates its superiority because it 1) is non-destructive; 2) collects more evidence than casts, especially when an impression is fragile (e.g. in dry fine sand); 3) requires less time and money to collect each piece of evidence, and 4) results in a digital file that can easily be shared with other examiners. This thesis describes the principle of the proposed technology, compares its performance with GOM ATOS Core 3D scanner, and presents our research findings using the prototype system developed.

# 2. METHOD

## 2.1 Introduction

High resolution automatic 3D measuring is very important in the advancement of evidence collection for forensic science, and a variety of other fields. Compare to conventional casting, it has the advantage of nondestructive, high speed, low cost, and results in a digital file that can be shared easily. This chapter will explain the principle behind the portable high-resolution automated 3D imaging system. The system consists of a camera and a projector. We use the pinhole camera model as the mathematical model for both the camera and the projector. Essentially, we need to find the corresponding point between the camera and the projector images in order to reconstruct the 3D geometry. We use digital fringe projection technique to project fringe patterns on the object and the phase-shifting algorithms to retrieve the phase information from the distorted fringe patterns. The auto-exposure and HDR algorithm make sure we captured high-quality fringe pattern images. Finally, the correspondence of each pixel is found with the phase information, then the 3D model is reconstructed with the pinhole model assumption.

## 2.2 Pinhole camera model

It is important to have an accurate mathematical model for the camera. While several camera models have been developed, the pinhole model is the most widely used model. We can see the camera as a mapping between the 3D world coordinate and the 2D image. So, our first goal is to find a matrix that could represent the camera projection.

$$u = PX \tag{2.1}$$

$u$ is the 2D image point, P is the projection matrix and $X$ is the 3D world point. As the geometry shown in figure 2.1, there are two coordinate systems and one plane, the camera coordinate, the world coordinate and the image plane. The camera coordinate, and the image plane lie in the world coordinate system. For now, we assume the origin of the camera coordinate coincides with the origin of the world coordinate.

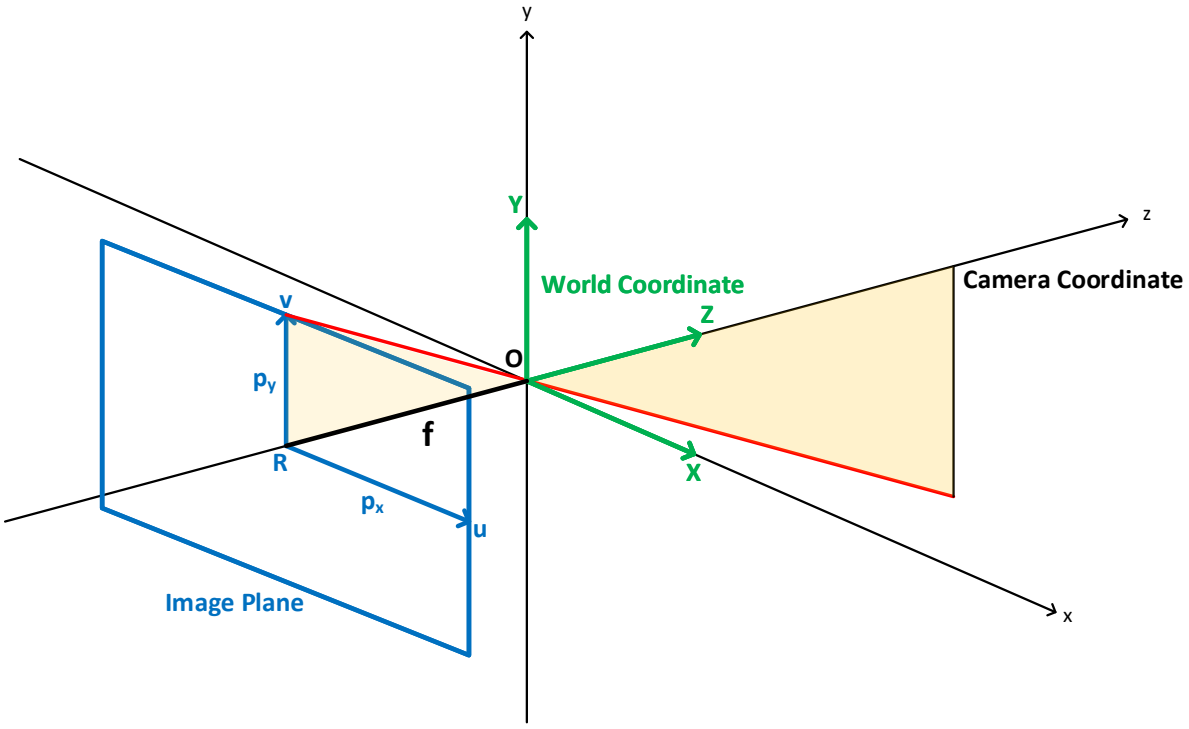


**Figure 2.1.** Geometry of a pinhole model.

We can derive the relationship between one pixel on the image plane with a point in the world coordinate using the similar triangle relationship.

$$\begin{bmatrix} u \\ v \end{bmatrix} = \frac{f}{Z} \begin{bmatrix} X \\ Y \end{bmatrix} \tag{2.2}$$

where $u$, $v$ are the 2D image coordinate and $X$, $Y$, $Z$ are the 3D world coordinate, and $f$ is the focal length of the camera in pixel distance. Furthermore, we can write down the whole generic camera model with focal length $f_x$, $f_y$, and scaling factor $s$.

$$s \begin{bmatrix} u \\ v \\ 1 \end{bmatrix} = \begin{bmatrix} f_x & 0 & 0 & 0 \\ 0 & f_y & 0 & 0 \\ 0 & 0 & 1 & 0 \end{bmatrix} \begin{bmatrix} X \\ Y \\ Z \\ 1 \end{bmatrix} \tag{2.3}$$

Usually, the camera origin and the image origin is different, so we have to include $P_x$, $P_y$ pixel numbers to account for it. While $P_x$, $P_y$ is usually half of the image width and height.

$$\begin{bmatrix} u \\ v \end{bmatrix} = \frac{f}{Z} \begin{bmatrix} X \\ Y \end{bmatrix} + \begin{bmatrix} P_x \\ P_y \end{bmatrix} \tag{2.4}$$

$$s \begin{bmatrix} u \\ v \\ 1 \end{bmatrix} = \begin{bmatrix} f_x & 0 & p_x & 0 \\ 0 & f_y & p_y & 0 \\ 0 & 0 & 1 & 0 \end{bmatrix} \begin{bmatrix} X \\ Y \\ Z \\ 1 \end{bmatrix} \tag{2.5}$$

Sometimes the camera does not share the same coordinate as the world. This is when the transformation matrices come in. The rotation matrix $R_{3\times3}$ and the translation matrix $t_{3\times1}$, transform the world coordinate into camera coordinate, so the equation expands to

$$s \begin{bmatrix} u \\ v \\ 1 \end{bmatrix} = \begin{bmatrix} f_x & 0 & p_x \\ 0 & f_y & p_y \\ 0 & 0 & 1 \end{bmatrix} \begin{bmatrix} R_{3\times3} & t_{3\times1} \end{bmatrix} \begin{bmatrix} X \\ Y \\ Z \\ 1 \end{bmatrix} \tag{2.6}$$

$$P = \begin{bmatrix} f_x & 0 & p_x \\ 0 & f_y & p_y \\ 0 & 0 & 1 \end{bmatrix} \begin{bmatrix} R_{3\times3} & t_{3\times1} \end{bmatrix}. \tag{2.7}$$

$$A = \begin{bmatrix} f_x & 0 & p_x \\ 0 & f_y & p_y \\ 0 & 0 & 1 \end{bmatrix} \tag{2.8}$$

$$K = \begin{bmatrix} R_{3\times3} & t_{3\times1} \end{bmatrix}. \tag{2.9}$$

$A$ is called the intrinsic matrix, and $K$ is called the extrinsic matrix. Now, we have a complete model that represents the relationship of a 3D point in the world with a pixel in the 2D image. Note that, with this equation, we can deduce 2D pixels from 3D points, but

not 3D points from the 2D pixels, since a 2D pixel could correspond to infinite 3D points on the same line.

As the projector is the inverse of the camera, the pinhole camera model still applies. If the camera and the projector are properly calibrated [31], [32], their respective projection matrices $P^c$ and $P^p$ were known. Thus, we can write down two equations, one for the camera and the other for the projector.

$$s^p \begin{bmatrix} u^p & v^p & 1 \end{bmatrix}^t = P^p \begin{bmatrix} X & Y & Z & 1 \end{bmatrix}^t \tag{2.10}$$

$$s^c \begin{bmatrix} u^c & v^c & 1 \end{bmatrix}^t = P^c \begin{bmatrix} X & Y & Z & 1 \end{bmatrix}^t \tag{2.11}$$

Here superscript p represents the projector and superscript c represents the camera. We assumed the world coordinate is aligned with the camera coordinate, so that leaves us 7 unknowns ($s^c$,$s^p$,$u^p$,$u^v$,$X$,$Y$,$Z$) and 6 equations. We will use the digital fringe projection technique and the phase-shifting algorithm following up to find the last constrain we need.

### 2.3 Digital fringe projection (DFP) technique

The DFP technique is a special type of triangulation-based structured light methodology where variations in pattern intensity are sinusoidal. This structured light method is similar to a stereo-based method, except that it uses a projector to replace one of the cameras [9]. Figure 2.2 is a schematic diagram of the DFP system. The projection unit (D), the image acquisition unit (E), and the 3D object (B) form a triangulation base. The projector images vertical (varying horizontally) binary straight fringe stripes (phase lines) on the object. The projector focus is adjusted so that the binary fringe stripes projected onto the object is slightly defocused. We then utilize the binary defocusing technique, so the binary patterns could approximate a sinusoidal pattern. The object's surface distorts the fringe images from straight phase lines to curved ones. A camera captures the distorted fringe images from another angle. In such a system, the correspondence is established by analyzing the distortion of the structured patterns (fringe) through fringe analysis techniques.

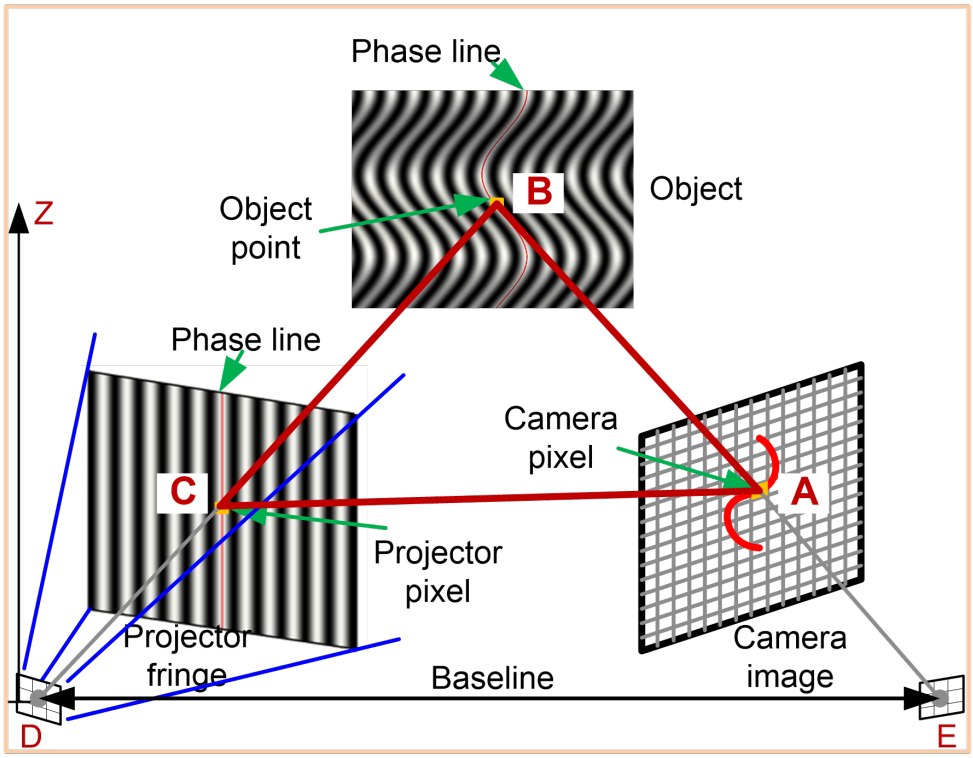


**Figure 2.2.** Schematic diagram of a 3D imaging system using a DFP technique [20].

## 2.4 Phase-shifting algorithm

Over the years, many fringe analysis techniques have been developed to retrieve phase information from fringe patterns. For example, the Fourier method, which needs only one fringe image, and various phase-shifting methods. However, phase-shifting methods are widely used because of their high speed, resolution, and accuracy [33]. There are several phase-shifting algorithms including three-steps, four-steps, multi-wavelength and N-steps least square, etc. For the purpose of capturing high-resolution static footwear and tire impression, N-steps least-square phase-shifting algorithm is deployed. In a phase-shifting technique, the sinusoidal fringe is shifted spatially from frame to frame with a known phase shift. The K-th fringe patterns can be mathematically described as

$$I_k(x,y) = I'(x,y) + I'' \cos\left[\phi(x,y) + \frac{2\pi k}{N}\right], \tag{2.12}$$

where $I'(x,y)$ is the average intensity, $I''(x,y)$ is the intensity modulation, $\phi(x,y)$ is the phase to be solved for, and $N$ is the total number of fringe patterns to be used which is 18 in this research. If the phase shift of the N-step phase-shifting algorithm is equal, simultaneously solving these N equations by a least square method yields

$$\phi(x,y) = -\tan^{-1}\frac{\sum_{k=1}^{N} I_k(x,y)\sin(\frac{2\pi k}{N})}{\sum_{k=1}^{N} I_k(x,y)\cos(\frac{2\pi k}{N})}, \tag{2.13}$$

Because of the arctangent function, the phase solved will be from $-\pi$ to $\pi$, which introduces a $2\pi$ discontinuity over every fringe period. In this case, we call the phase "wrapped phase". The $2\pi$ discontinuities are removed by employing a 2D temporal phase-unwrapping algorithm, gray coding phase unwrapping. The phase unwrapping step essentially finds the $2\pi$ jumps and removes them by adding or subtracting an integer fringe order M of 2pi to the appropriate region, that is, the unwrapped phase

$$\Phi(x,y) = \phi(x,y) + 2\pi \times M. \tag{2.14}$$

The whole point of finding the phase information is to find the corresponding point of the camera image to the projector image. We already know the phase information of the projector, since we know the fringe patterns we project. We also know the phase information of the camera image, which we just solved above from the images captured. If we can find the pixel in the projector image which has the same phase value as the pixel in the camera image, we then find the corresponding point. The relationship between the corresponding projector pixel $u_p$ and camera pixel $u_c$,$v_c$ is obvious now.

$$u^p = \frac{\phi(u^c, v^c)}{2\pi} \times P \tag{2.15}$$

P is the number of pixels per fringe period. This is the last constrain we need to solve equation 2.10 and 2.11! The 3D coordinates can then be recovered now.

Furthermore, analyzing the same set of fringe images yields a texture image $I^t$ (i.e., a photograph of the object without fringes) as

$$I^t(x,y) = \frac{1}{N}\sum_{k=1}^{N} I_k(x,y). \tag{2.16}$$

Note that the texture image is perfectly aligned with the 3D points generated from the phase map. Therefore, for each 3D point, the texture (RGB color and intensity) information can be directly extracted, and vice versa. In general, the more phase-shift steps used, the higher the quality of the phase, but the slower the measuring speed becomes. The N-step phase-shifting algorithm has the following advantages: 1)Less sensitive to surface reflectivity variations. The phase value of a point is computed via the arctangent function. As the reflectivity of each pixel is constants during the measurement, they will be canceled out. 2)Immune to ambient light influences. The phase-shifting method analyzes the phase information instead of the intensities. 3)High spatial resolution. Since the phase of each pixel is computed, the 3D measurement can be performed at camera pixel spatial resolution. 4) Can achieve high measurement accuracy. If proper calibration is performed, sub-pixel correspondence of the camera and the projector can be established, thus achieve high measurement accuracy. 5)Permit high-speed 3D measurement. A minimum of 3 phase-shift steps is needed to reconstruct a 3D model. In addition, a scene to be measured needs to be scanned and processed only once. Multiple scans of the scene are not required, therefore permits fast 3D measurements. However, the projector controls the projection intensity by time modulation. (ref) Therefore, when 8-bit sinusoidal fringe patterns are being projected, the conventional DFP-based 3D imaging techniques have the following major limitations [34]: 1) precise timing control between the camera and the projector is required; 2) sensitivity to the projector's nonlinear response and 3) low fringe contrast(because of nonlinear response). These difficulties can be overcome by applying the binary defocusing technique. Figure 2.3 shows 3 of the 18 step phase-shift patterns we used in this research. Figure 2.4 demonstrates the process of fringe analysis from fringe images to the wrapped phase information and the texture image.

## 2.5 Gray coding phase unwrapping

Gray coding phase unwrapping algorithm is a kind of temporal phase unwrapping method. It is an improved version of the simple coding phase unwrapping algorithm. In the simple

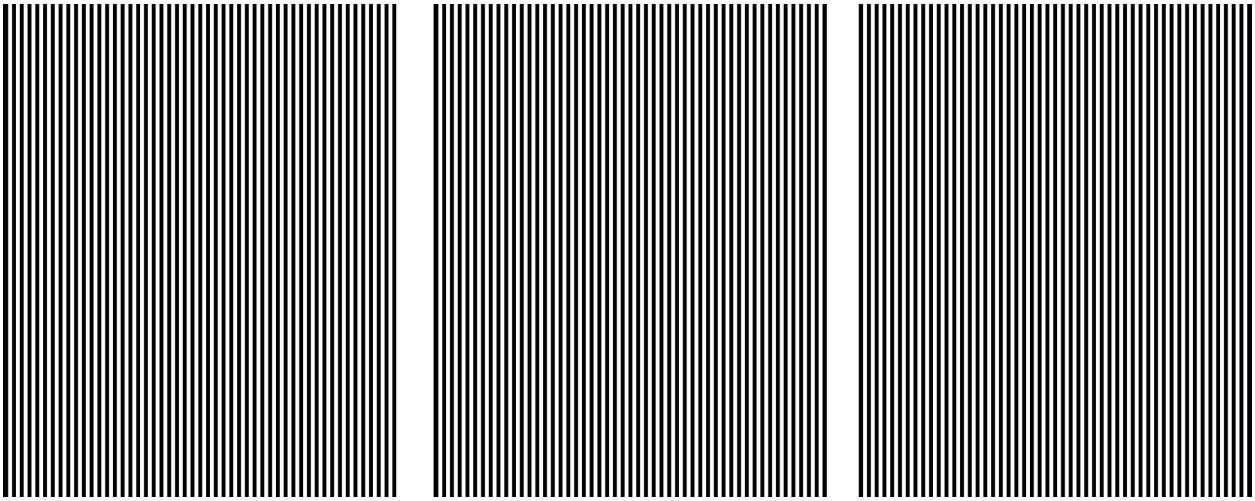

**Figure 2.3.** Three of the 18 fringe patterns used in phase-shifting algorithm.

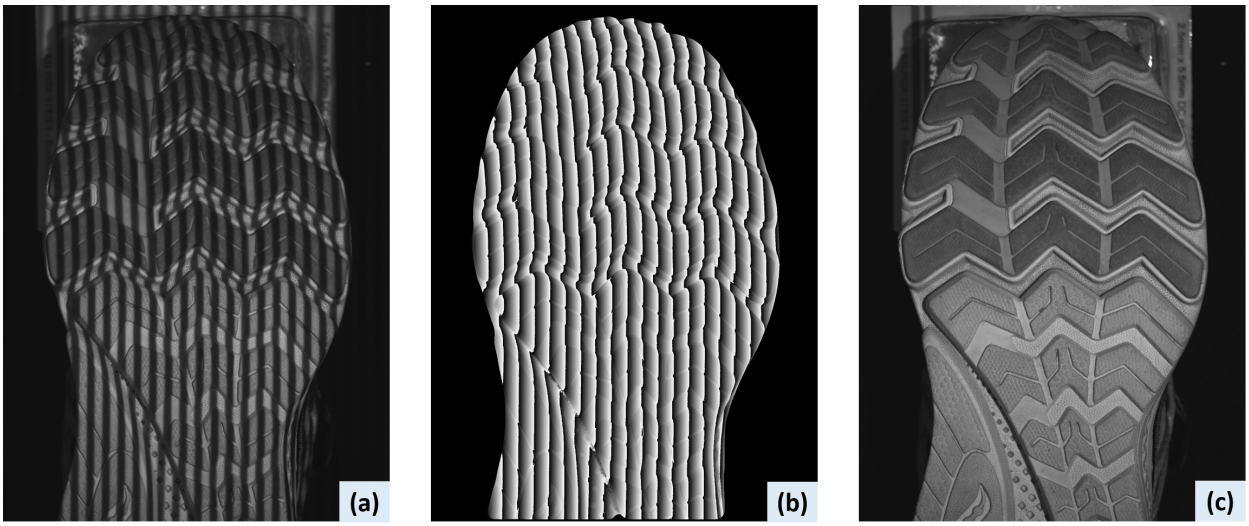


**Figure 2.4.** The process of the fringe analysis. (a) Image of the first of the eighteen fringe patterns projected onto a shoe bottom; (b) wrapped phase information of the shoe bottom retrieved from the fringe images captured; (c) texture image of the shoe bottom retrieved from the fringe images captured.

coding algorithm, binary patterns with binary changes aligned to the $2\pi$ phase discontinuities are projected onto the object and then captured by the camera. These binary patterns form unique codewords for each fringe period, consequently, the fringe order M of every fringe period can be decoded. Recall from the last section, using equation 2.14, the unwrapped phase can be obtained. However, in a real situation, the binary patterns projected and captured will not have a clean edge (grayscale value 0/255 or 255/0) on every binary digit.

Hence, it will easily create fringe order ambiguity on the edge of each fringe period when two successive fringe order values differ in multiple binary digits.

Gary coding increases the robustness of simple coding by using a special binary order that two successive fringe order values differ in only one binary digit. From this approach, the codeword-detecting error can be reduced and the unwrapped phase result can be improved. Figure 2.5 shows the comparison of the binary coded patterns for fringe order determination between simple coding and gray coding algorithm and figure 2.6 shows the first 3 of the 6 gray code patterns we used in this project. Figure 2.7 demonstrates the process of gray coding phase unwrapping from gray coding images to the wrapped phase information and the unwrapped phase information. Figure 2.8 shows the process of unwrapping the phase with the gray coding algorithm.

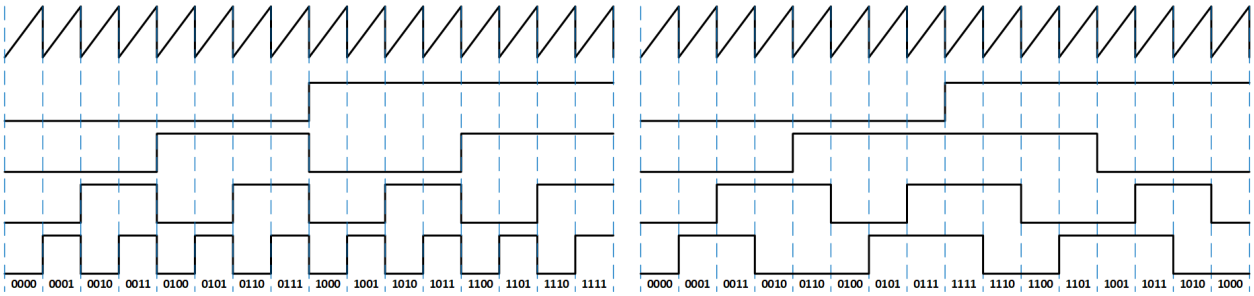


(a) (b)

**Figure 2.5.** (a) Simple coding; (b) gray coding. The first row is unwrapped phase from $-\pi$ to $\pi$, the bottom three rows are the binary codes. Note that in gray coding, there is only one binary bit change between codewords.

## 2.6 Binary defocusing technique

To compensate for human vision, the conventional digital projector usually includes non-linear gamma compensation. Therefore, in order to perform high-quality 3D measurement with digital fringe projection technique and phase-shifting algorithm, gamma correction is usually mandatory. Gamma correction can be done by actively changing the fringe pattern to be projected or compensating for the phase error. However, the output intensity doesn't change much when it is close to 0 or 255 and the nonlinear gamma actually changes over time. So, it is almost impossible to generate sinusoidal fringe images with correct grayscale

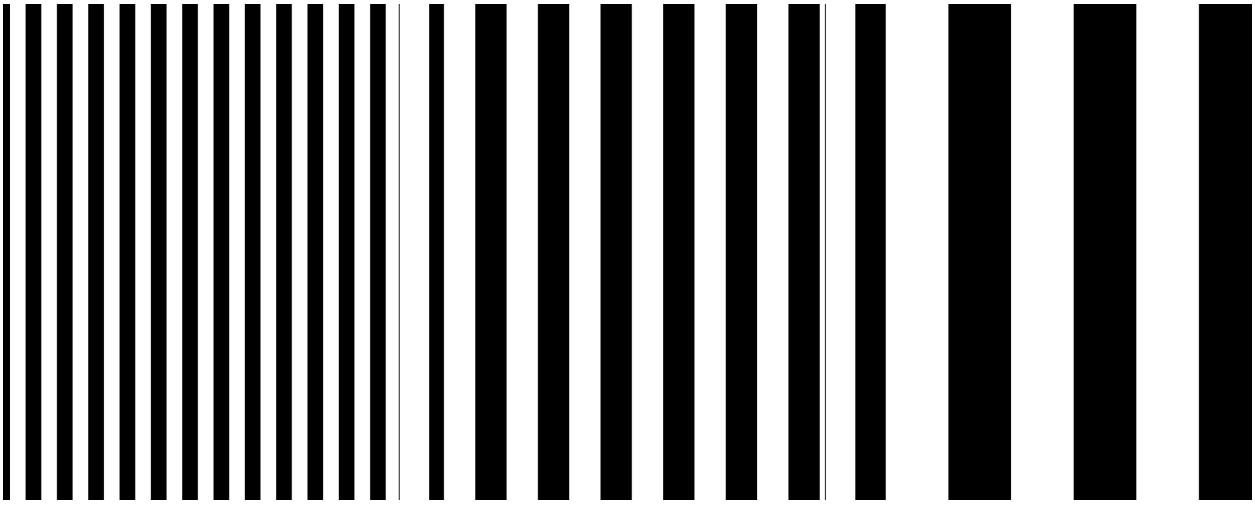

**Figure 2.6.** First 3 of the 6 gray code patterns we used.

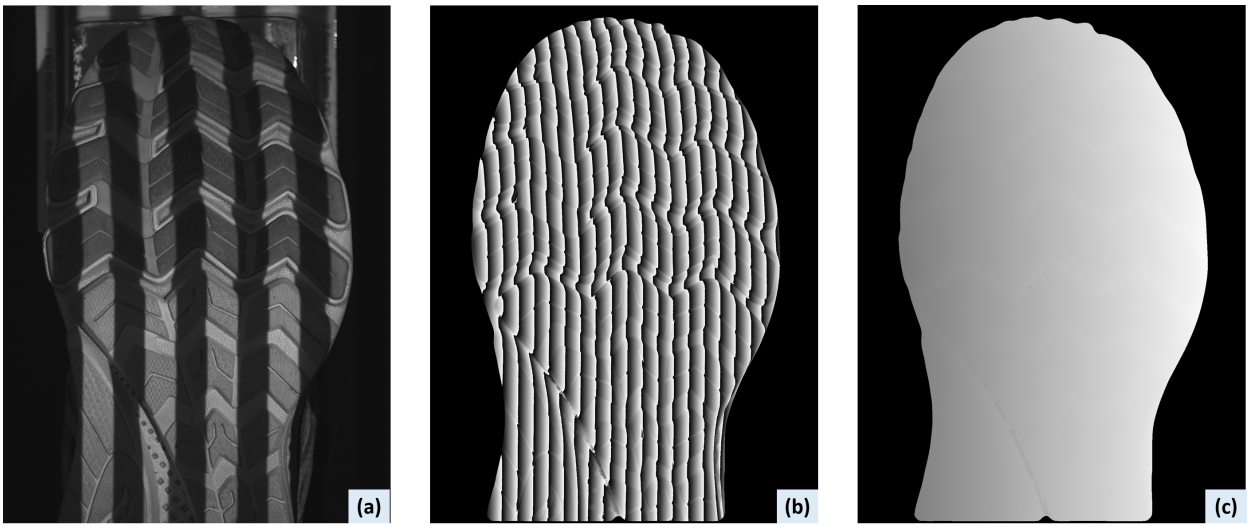


**Figure 2.7.** The process of the gray coding phase unwrapping. (a) Image of the first of the six gray code patterns projected onto a shoe bottom; (b) wrapped phase information of the shoe bottom retrieved from the fringe images captured; (c) unwrapped phase information obtained by unwrapping the wrapped phase information using gray coding algorithm.

value 0 ~ 255. Instead of using 8-bit (grayscale value 0 ~ 255) fringe patterns, the binary defocusing technique only utilizes 1 bit (grayscale value 0 and 255) binary patterns. The sinusoidal patterns are generated by defocusing the binary patterns and are projected onto the object. From the experiment results, the binary defocusing method and the traditional gamma correct sinusoidal method reach similar phase error [26].

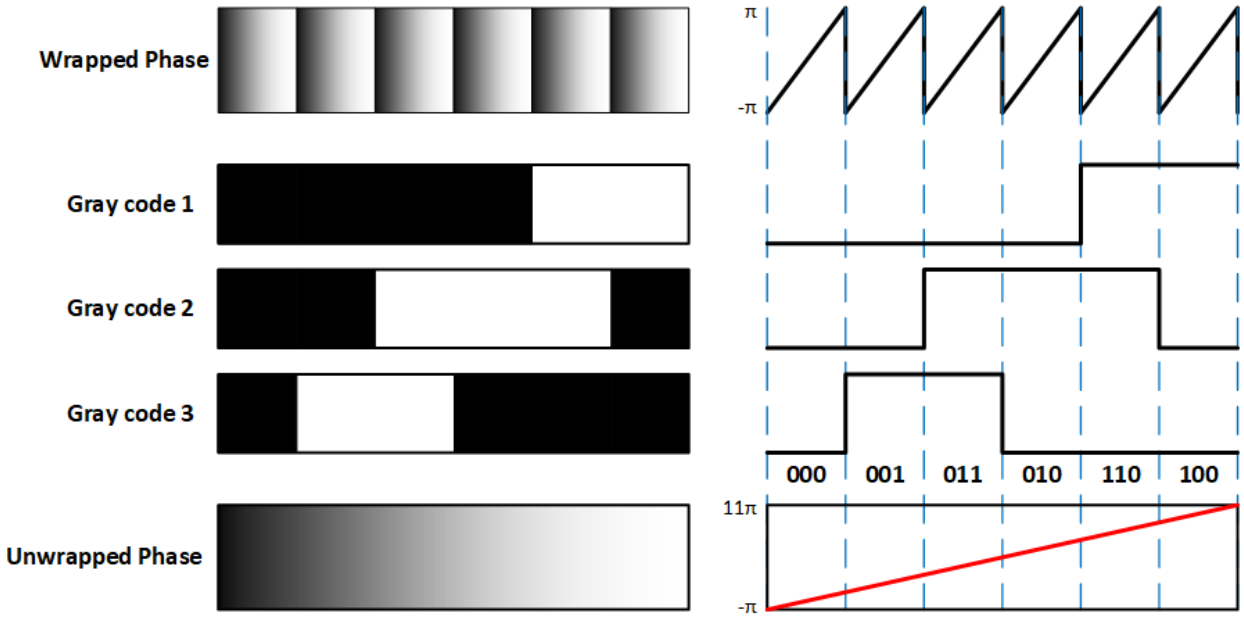


**Figure 2.8.** Schematic diagram of the process of unwrapping the wrapped phase with gray coding algorithm.

Furthermore, the core of a digital light projector is the digital-micro mirror device(DMD). The ON and OFF of each pixel are controlled by rotating the micromirror. The projector controls the ON time ratio in each projection period to achieve gray-scale value 0~ 255. For example, if the projector is projecting at 60Hz and at a gray-scale value of 128. The projection period will be 1/60s and the ON time will be 1/120s. Therefore, in order to obtain the correct gray-scale value of each pixel in a sinusoidal pattern, the camera exposure time must be precisely the multiple of the projection period. By projecting only binary patterns (grayscale values 0 and 255), the binary defocusing technique [26] overcomes the major limitations of the conventional DFP method while maintaining the merits of the fringe analysis method.

This approach, therefore: 1) does not require precise timing control (since each DLP micro-mirror remains stationary during the projection period), thus, any partial time segment can represent the projected pattern, allowing for arbitrary camera exposure times [26]; 2) is immune to projector's nonlinear response [26], and 3) has the highest possible contrast (purely black and purely white) [35]. In addition, the binary defocusing technique allows

the flexible exposure time choice that enables the auto-exposure we have developed [36]. In summary, our 3D imaging system employs the binary defocusing technique due to its overwhelmingly advantageous features.

### 2.7 Auto-exposure time control

High-resolution and high-speed 3D measurement devices utilizing DFP technique have been extensively studied and developed. When applying those devices to various fields, the automation process becomes significantly important. Because the automation process enables non-experts to consistently acquire high-quality data without profound knowledge in DFP technique. Auto-exposure time control according to the scene in the field of view has been commonly used in 2D imaging devices. On the contrary, due to the limitation of the conventional DFP method, the auto-exposure time control in 3D measurement base on the DFP technique has much less development.

In order to adjust the image intensity in a DFP system, there are basically five ways. 1) Adjust the camera aperture. 2) Adjust the projector aperture. 3) Adjust the projector light intensity. 4) Change the camera gain. 5)Adjust the camera exposure time. The first two methods involve manually adjusting the physical components of the DFP system. This is not desirable, since any movement of the camera or the projector will require the system to be re-calibrated. The third method is also not feasible either because it requires precise time control of the camera exposure time as mentioned in the last subsection. We also tend to maintain camera gain as 1 because this way the noise will not be amplified and the signal-to-noise ratio will be the highest.

On account of the binary defocusing technique, an efficient optimal exposure time determination method was developed, and the method was also extended to a High Dynamic Range (HDR) algorithm [37]. These algorithms were developed based on two findings: 1) the intensity of the image acquired by a camera is approximately linearly related to the camera exposure time when the camera is responding properly (i.e., no saturation); and 2) the offset of the response curve ($c_0$) is a fixed value for a given camera setting (e.g., gain, lens, aperture). After pre-calibrating the camera's linear response function, these findings

allow us to determine a global optimal exposure time ($t^o$) by capturing one single image with proper exposure $t_0$ (e.g., no saturation). The optimal exposure time $t^o$ is determined by

$$t^o = \frac{I_{max}(t_0) - c_0}{I_m(t_0) - c_0} \times t_0 \tag{2.17}$$

Where $I_{max}$ is the maximum desired pixel intensity value for the final image, $I_m(t_0)$ is the $m$ percent intensity value of the image taking with known proper exposure time $t_0$, $c_0$ is the pre-calibrated response offset and $t^o$ is the optimal exposure time we want. Since only a single exposure is used, our auto-exposure control algorithm is very fast. Furthermore, a novel method was developed to automatically determine the optimal exposure times required to achieve HDR by analyzing the image captured with the global optimal exposure time (preferably for better prediction) or the same image used for global exposure time determination.

Figure 2.9 shows representative experimental results of a high-contrast scene utilizing our HDR technique. Figure 2.9(a) shows the scene with two shoes having different brightness levels. With a single exposure, one can only capture one part with high quality. For example, if the exposure time is optimized for the right shoe, as shown in Figure 2.9(b), the bright left shoe shows poor quality due to saturation. Figure 2.9(c) shows the result if the exposure is optimized for the left shoe, the right shoe has a lower signal-to-noise ratio (SNR) and thus details are not clear. Our HDR technique properly captures both shoes with high quality, as shown in Figure 2.9(d). To better visualize the difference, we created close-up views of the dark shoe. The HDR image shows less random noise, indicating a higher quality image was captured. These images are shown in Figure 2.9(e)(f).

## 2.8 Summary of 3D reconstruction process

First, the camera and the projector are been calibrated to obtain their intrinsic matrices and the extrinsic matrix. Then, DFP technique is deployed to obtain the last constrain we need to solve equation 2.10 and 2.11. We project and capture 18 phase-shifting binary fringe patterns and utilize binary defocusing technique to retrieve the wrapped phase information of the measuring object. Additional 6 gray code patterns are also been projected and captured

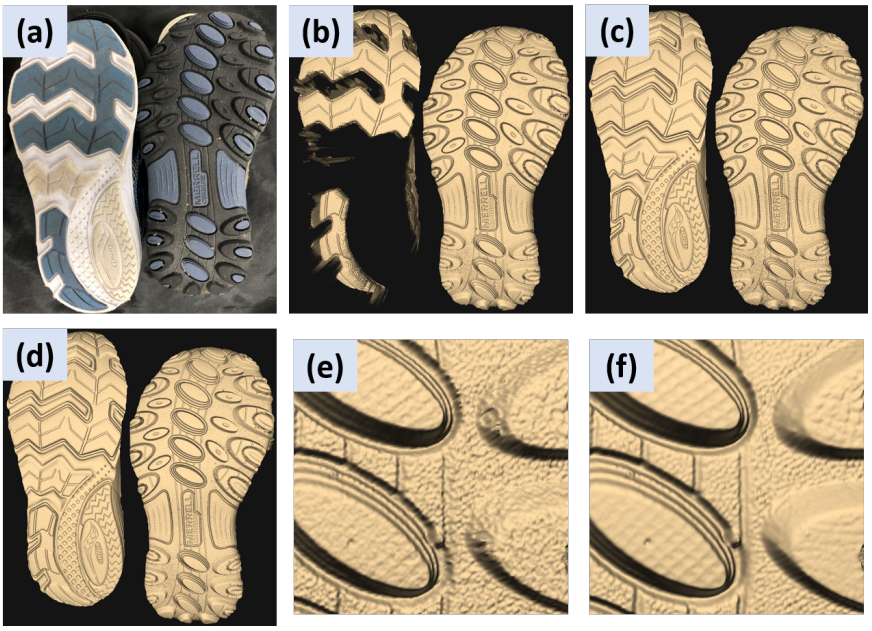


**Figure 2.9.** Experimental results using our developed HDR algorithm. (a) Photo of the scene; (b) 3D result with an optimized exposure time for the right shoe; (c) 3D result with an optimized exposure for the left shoe; (d) 3D result with the HDR algorithm using three exposures; (e) Close-up view of the 3D result of the right shoe with an optimized exposure for the left shoe; (f) Close-up view of the 3D result of the right shoe with the HDR algorithm using three exposures.

to unwrap the wrapped phase information. Finally, we combine 2.10, 2.11 and 2.15 to recover 3D. Figure 2.10 shows the process of 3D reconstruction.

## 2.9 Prototype Systems

A fully automated 3D imaging system was developed to allow the user to easily and quickly capture high-resolution shoe and tire impressions. The system's hardware was designed to be portable and easy to set up, and the system's software graphical user interface (GUI) was designed to be intuitive to operate without training.

Simple hardware design for easy setup and operation: The prototype system is portable and can be packed into Pelican 1450 Case (interior dimension 371.3mm × 258.6mm × 152.4mm). Figure 2.11(a) shows the prototype system. The system can be set up quickly with four steps for data capture: 1) plug in the power cord; 2) connect the USB cable be-

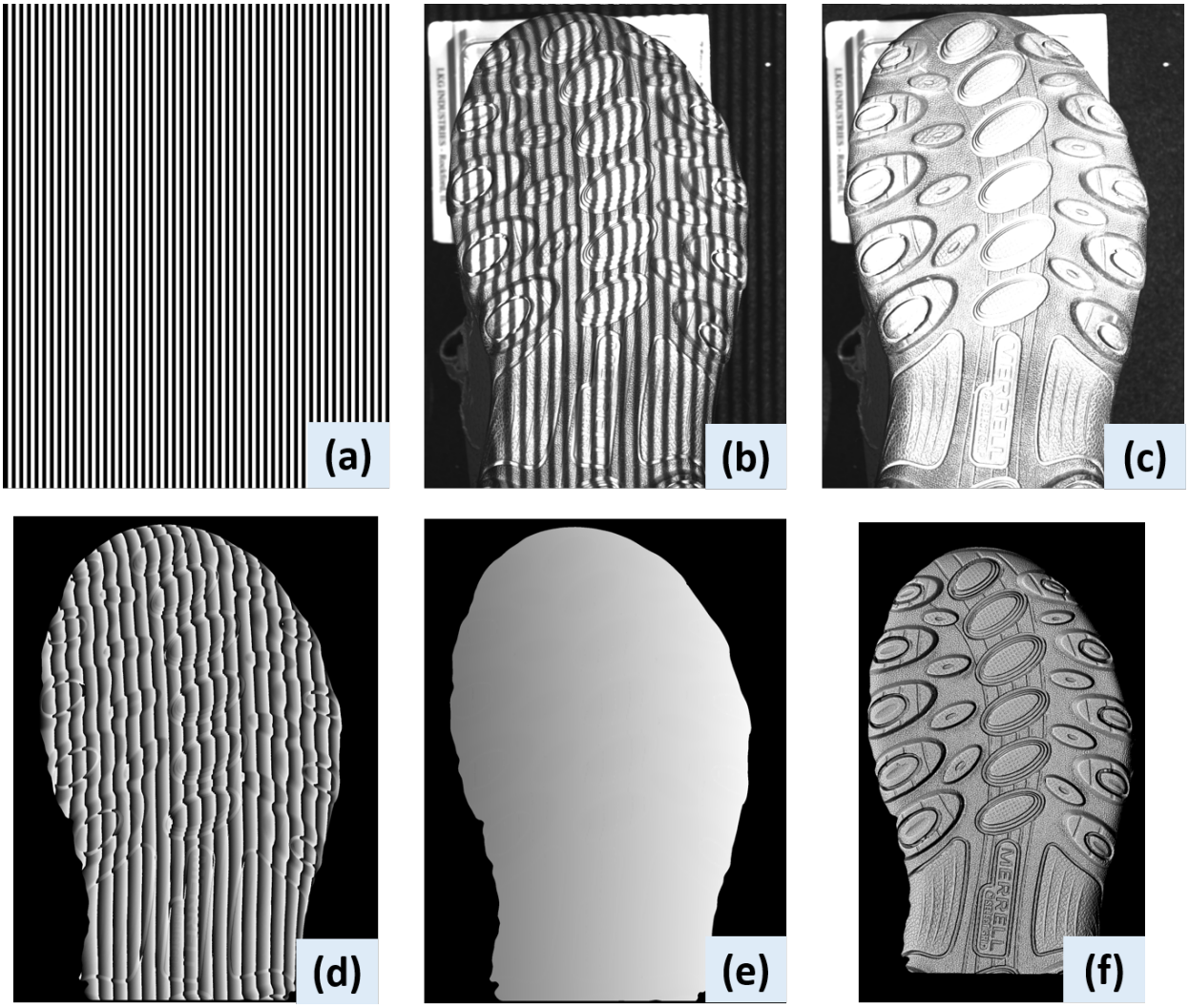


**Figure 2.10.** The process of 3D reconstruction. (a) 1 of the 18 Phase-shifting fringe patterns; (b) image of a fringe pattern being projected onto a shoe bottom; (c) texture image of the shoe bottom obtain from equation 2.16; (d) wrapped phase information retrieve from the fringe patterns; (e) unwrapped phase information obtain by using gray coding algorithm; (f) the reconstructed 3D model of the shoe bottom.

tween the device and a laptop computer; 3) toggle the power switch on; 4) start the software for data capture.

Software graphical user interface (GUI) design for ease of use: Figure 2.11(b) shows the software GUI to operate our prototype system. The software was designed to be intuitive such that no training is necessary to operate our prototype system. The prototype system was sent without instructions to Mr. William Henningsen at the Omaha Police Department and

his team had no problem properly operating the system for high-quality data capture (Mr. William Henningsen, personal communication, Aug 10, 2020). The system was also used in workshops at International Association for Identification (IAI) and Illinois Association for Floodplain and Stormwater Management (IAFSM) conferences, and those in attendance reported in workshop surveys that the software is easy to use.

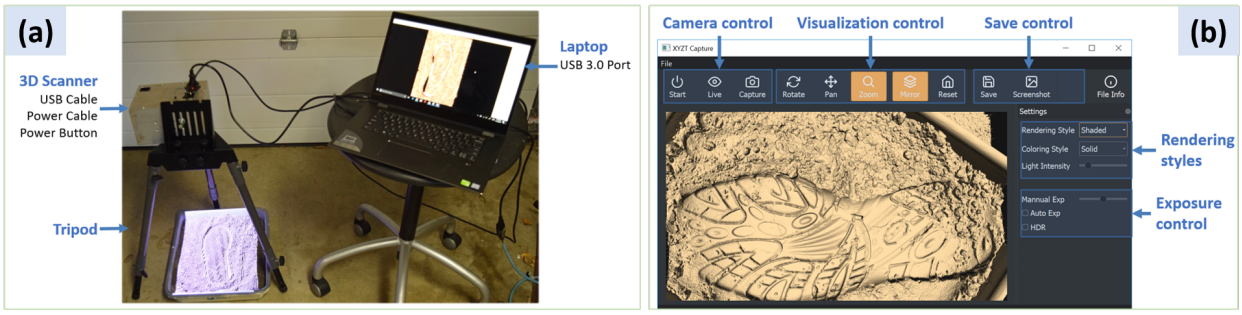


**Figure 2.11.** Our portable 3D imaging prototype. (a) Hardware system; (b) software GUI.

Two prototype systems were developed for evaluations: high resolution and low resolution. The high-resolution system achieves approximately 400 dpi with a FOV of 5.12" × 3.84" (130.05mm × 97.54mm). The low-resolution system achieves approximately 137 dpi with a field of view (FOV) of 14" × 8.75" (355.6mm × 222.25mm). The prototype system includes a complementary metal-oxide-semiconductor (CMOS) camera and a digital light processing (DLP) projection device (LightCrafter 4500, $1299 USD). An Arduino board (Arduino Uno, $23 USD) is used to trigger the camera and the projector simultaneously. The projector's resolution is 912 ×1140 pixels. The low-resolution prototype system uses a CMOS camera with a resolution of 1920 × 1200 pixels (FLIR Grasshopper3 GS3-U3-23S6M, $1250 USD), and the camera is attached with a 16 mm lens (Computar M1614-MP2, $119.95 USD). The high-resolution system uses a CMOS camera with a resolution of 2048 × 1536 pixels (FLIR Grasshopper3 GS3-U3-32S4M, $1150 USD) that is attached with a 25 mm lens (Computar V2528-MPY, $379.99 USD). After including the cost of the power adaptor and the manufacturing, the total cost of the system is approximately $3000 USD, which is less than one-tenth of the GOM ATOS CORE system. For all evaluations, the system projects

and captures fringe images at 60 Hz. Figure 2.12 shows the interior of a high-resolution system.

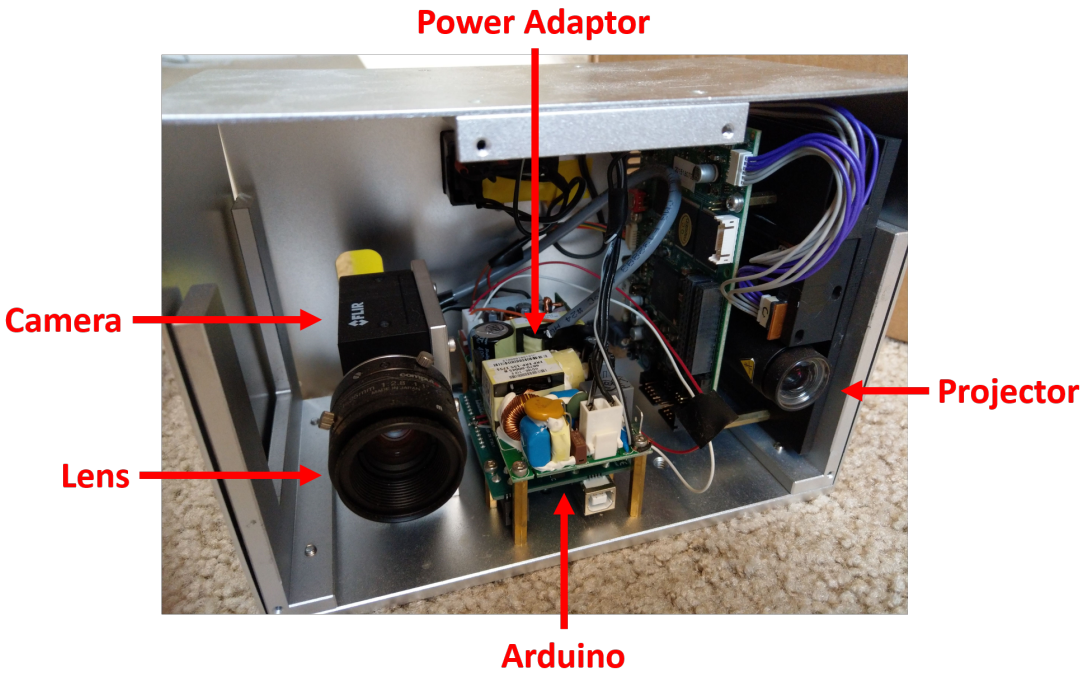


**Figure 2.12.** Interior of a high-resolution system.

## 2.10 Experiments setup

The distance between the camera sensor in the prototype system and the measuring surface, which we call it the measuring distance, is designed to be around 0.5 meters. Therefore, We mount the prototype systems on the tripod, so they can be set up above any impressions on the ground, and the measuring distance can be adjusted by stretching the tripod's legs. Before capturing 3D, we adjust the measuring distance to make the measuring surface as focus as possible for the camera. But the projector has to be slightly defocused so that we can take the advantage of the binary defocusing technique. Then, we use the GUI we developed to adjust the exposure time manually or using the auto-exposure time control and HDR algorithm to make sure we capture high-quality fringe images. Finally, the 3D model is captured by one click on the capture button in the GUI. Figure 2.13 shows the setup of the prototype system above a shoe impression in the snow.

**Figure 2.13.** Prototype system set up above a shoe impression in the snow.

# 3. RESULTS AND DISCUSSION

## 3.1 Introduction

In this chapter, both the high-resolution system and the low-resolution systems are put to the test. The performance of both systems is compared with the high end commercial 3D scanner (GOM ATOS CORE). The system accuracy of all systems is first evaluated by measuring a plane surface in 8 different poses. Then, the system resolutions are inspected by measuring 2 shoe bottoms and impressions in 3 different substrates. Because the GOM system uses blue structure light while our prototype systems use white structure light, a sphere painted with red, green, and blue color is measured to evaluate the influence of color on each system. Finally, our prototype systems are sent to the forensic scientist, Mr. James Wolfe, to compare the performance of 3D imaging to traditional 2D evidence quality photographs and physical casts by capturing impressions in clay, damp sand, damp fine silt, dry snow, and most importantly wet snow.

## 3.2 System accuracy evaluation

Our high-resolution and low-resolution prototype systems were compared against a commercially available high-end 3D optical measurement device (GOM ATOS CORE). The accuracy of each system was evaluated by measuring a planar surface (the backside of a mirror) at 8 different poses with different positions and orientations. Figure 3.1 shows one of the poses set up for the GOM system, the low-resolution system, and the high-resolution system.

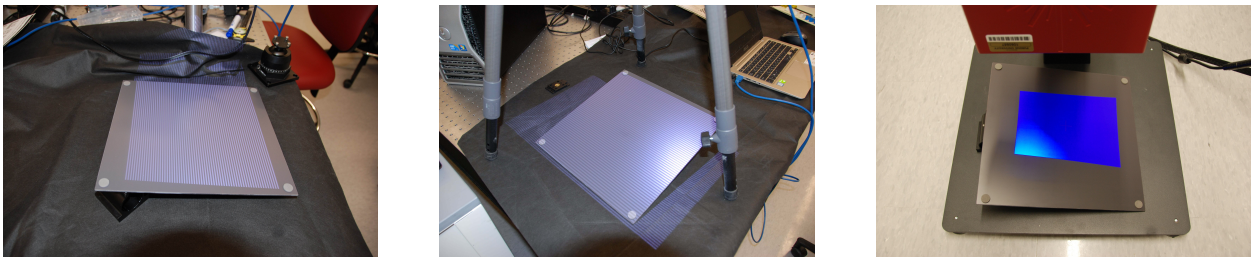

(a) (b) (c)

**Figure 3.1.** One pose setup of the (a) low-resolution system; (b) high-resolution system; (c) GOM system.

A compensation algorithm is deployed to deal with the small distortion and tilt of the 3D model reconstructed by our prototype systems because of the inevitable error during system calibration. First, we capture the planar surface on a completely flat pose (lying on the optic table). We then use the MATLAB function "fit" to help us fit a linear polynomial surface to the data points and use it as an idea reference surface. The error map of the reference surface is generated by subtracting the data points with the fitted ideal reference surface. Figure 3.2 shows the flat pose setup, the fitted ideal reference surface with the original data points, and the error map of the reference surface. For all the measurements below, the captured data points are compensated with the reference surface and the reference error map.

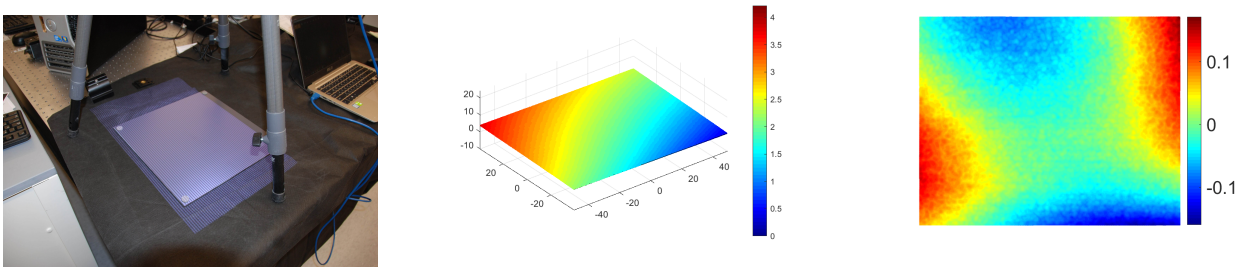


(a) (b) (c)

**Figure 3.2.** (a) Flat pose setup; (b) fitted ideal reference surface with the original data points (units: mm); (c) error map of the reference surface (units: mm).

An error map for each measurement was created by fitting the measured and compensated data with an ideal plane and taking the difference between the measured data and the ideal plane. We try to take as high percentage of the field of view as possible into account. Therefore, an image area of $100 \times 80\, mm^2$ for the GOM and our high-resolution system, and $200 \times 160\, mm^2$ of our low-resolution system was taken from the center of each measurement for analytical evaluation. A Gaussian filter with a size of $5 \times 5$ pixels and a standard deviation of 5/3 pixels was applied to data from our systems to reduce the most significant random noise. Figure 3.3 shows error maps of 1 of the 8 poses measured by all three systems.

The root-mean-square (rms) value of each error map was calculated with the following equation.

$$RMS\, value = \sqrt{\frac{1}{N}\sum_{k=1}^{N}(z_{o_k} - z_{\mathrm{i}_k})^2} \tag{3.1}$$

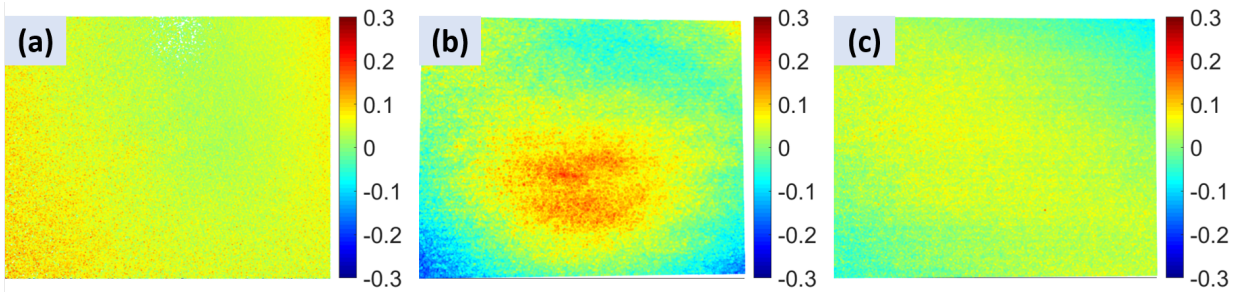


**Figure 3.3.** Error maps for planar surface measurement (units: mm). (a) Error map of the data measured by the GOM system (rms: 0.031 mm); (b) error map of the data measured by our low-resolution system (rms: 0.057 mm); (c) error map of the data measured by our high-resolution system (rms: 0.031 mm).

Where N is the total number of pixels, $z_o$ is the depth values of the measured data and $z_{\mathrm{i}}$ is the depth values of the ideal plane.

Table 3.1 summarizes the results. These experimental data show that: 1) for the same area size our high-resolution system captures more data points than the GOM system despite these two systems have a similar resolution (dpi), and we believe that GOM system discards a lot of data points for unknown reasons; 2) our high-resolution system achieved slightly higher measurement accuracy than the GOM system for most cases (smaller rms error); 3) our lower-resolution system accuracy is lower than the GOM system, but the difference is very small: only in tens of micrometers.

The system accuracy was further evaluated by measuring a sphere with a diameter of $80\,mm$. For each measurement, the data were fitted to an ideal sphere with a diameter of $80\,mm$. The ideal sphere is found by first estimating the center of the data points then creates the sphere around it. By finding the minimum value of the following equation, the point that has the smallest distance with all the data points can be found, thus the estimated ideal sphere center.

$$r_{o_{\mathrm{i}}} = \sqrt{(x_{o_{\mathrm{i}}} - x_{\mathrm{e}})^2 + (y_{o_{\mathrm{i}}} - y_{\mathrm{e}})^2 + (z_{o_{\mathrm{i}}} - z_{\mathrm{e}})^2} \tag{3.2}$$

$$\sum_{\mathrm{i}=1}^{N} [r_{o_{\mathrm{i}}} - r]^2 \tag{3.3}$$

**Table 3.1**. Root-mean-square (rms) error and the number of data points measured by each system for a planar surface measured at 8 different poses.

| | GOM | | Low resolution | | High resolution | |
|---|---|---|---|---|---|---|
| **Pose** | **# of points** | **rms (mm)** | **# of points** | **rms (mm)** | **# of points** | **rms (mm)** |
| #1 | 1074847 | 0.031 | 790268 | 0.056 | 1697702 | 0.031 |
| #2 | 1204415 | 0.030 | 790268 | 0.057 | 1697702 | 0.025 |
| #3 | 952446 | 0.032 | 790268 | 0.042 | 1697702 | 0.019 |
| #4 | 1330323 | 0.028 | 790268 | 0.054 | 1697702 | 0.024 |
| #5 | 1182172 | 0.031 | 790268 | 0.047 | 1697702 | 0.032 |
| #6 | 1118997 | 0.032 | 790268 | 0.057 | 1697702 | 0.031 |
| #7 | 1004454 | 0.032 | 790268 | 0.045 | 1697702 | 0.029 |
| #8 | 1047721 | 0.031 | 790268 | 0.039 | 1697702 | 0.022 |
| Mean | 1114428 | 0.031 | 790268 | 0.050 | 1697702 | 0.027 |

$r_o$ is the distance from a data point to the estimated center, $x_{o_i}$, $y_{o_i}$, $z_{o_i}$ are the x, y, z coordinate of the data points, $x_e$, $y_e$, $z_e$ is the x, y, z, coordinate of the estimate ideal sphere center, N is the total number of data points and r is the ideal sphere radius, which is $40\,mm$. To further increase the accuracy of the estimated ideal sphere center, the center is been estimated twice. We filter out the noise that is too far ($r_o > 40.5\,mm$) from the center at the first estimation, then we do the second fine estimate to obtain the accurate estimate sphere center. The same portion of the 3D model, $20\,mm$ from the top of the sphere, is taken from 3 measurements for evaluation. The error map was created by taking the difference between the measured data and the ideal sphere. A Gaussian filter with a size of $5 \times 5$ pixels and a standard deviation of 5/3 pixels was applied to our data to reduce the most significant random noise. Figure 3.4 shows the results of this experiment, again comparing all three systems.

As before, the rms value for each error map was calculated to quantitatively compare the differences that are summarized in Table 3.2.

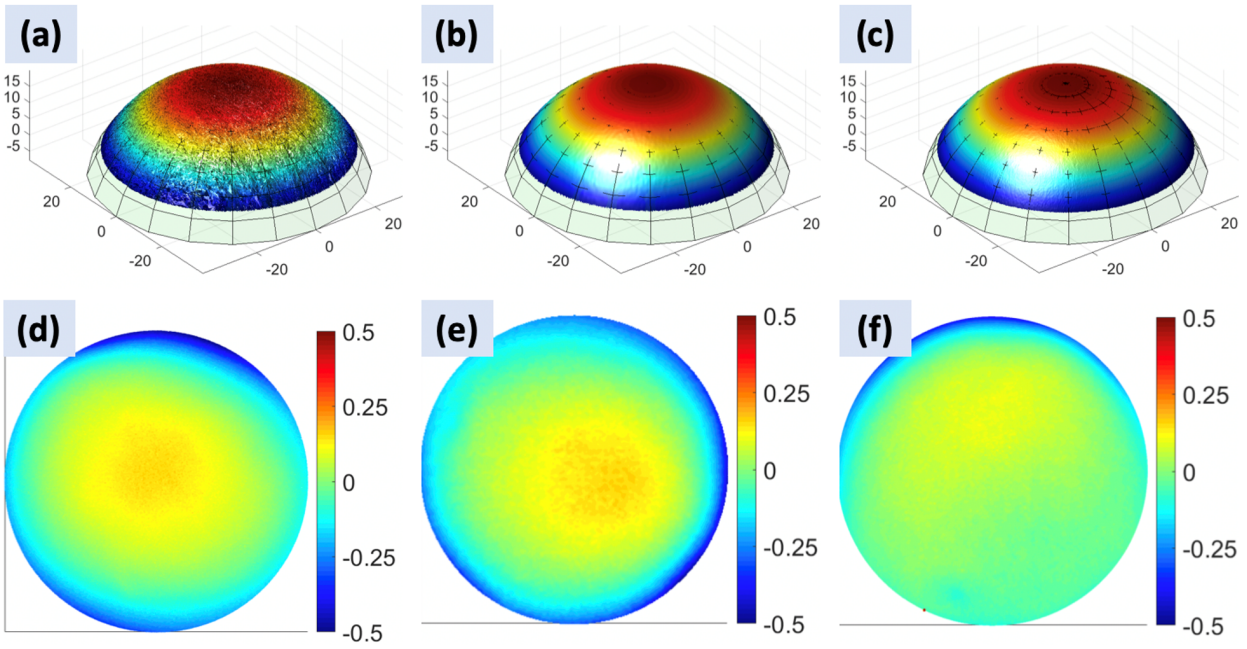


**Figure 3.4.** Measurement results for a sphere with a diameter of 80 mm. (a) Overlap 3D data obtained by the GOM system and the ideal sphere; (b) overlap 3D data obtained by our low-resolution system and the ideal sphere; (c) overlap 3D data obtained by our high-resolution system and the ideal sphere; (d) error map of (a) (rms: 0.117 mm); (e) error map of (b) (rms: 0.125 mm); (f) error map of (c) (rms: 0.070 mm).

$$RMS\,value = \sqrt{\frac{1}{N}\sum_{i=1}^{N}(r_{o_i} - r)^2} \tag{3.4}$$

**Table 3.2**. The rms error and the number of points measured by each system for the sphere-fitting experiment

| | **GOM** | **Low resolution** | **High resolution** |
|---|---|---|---|
| # of points | 619634 | 97978 | 822864 |
| rms error (mm) | 0.117 | 0.125 | 0.070 |

Once again, our high-resolution system achieves higher measurement accuracy with more data points than the GOM system, and our low-resolution system is slightly less accurate than the GOM system. The sphere examples have higher rms errors because of several reasons. First, its geometry variation is more than the plane. The fringe patterns projected

onto the sphere can be highly distorted, thus leading to less precise phase information. Second, we fitted the ideal sphere with the measured data points, so the estimated ideal sphere center may not be the actual sphere center although we try to estimate it as accurately as possible by estimating it twice. Also, the measured data points are most likely not forming a perfect sphere. Third, the sphere object we used is slightly reflective, therefore, the signal to noise ratio is higher. The above two experiments confirm that our proposed method can achieve 3D measurement quality similar to, or better than, that of the GOM system, depending upon the accuracy of the system.

### 3.3 System resolution evaluation

The resolution of these systems was evaluated by measuring objects with detailed features. Figure 3.5 shows the light shoe bottom while being measured. A region of shoe bottom shown in Figure 3.6(a) was measured by all systems. All captured 3D files were converted to the *.STL format (a format used by the GOM system), and then loaded into the open-source visualization software package MeshLab (http://www.meshlab.net). Figure 3.6(b)-(d) shows the rendered images. The result of the high-resolution system and the GOM system clearly show small grid and hexagon shape indents that have a size under 2mm, and they even capture the smallest dot patterns which have a size under 1mm. Our observations from these test are: 1) our high-resolution system resolves all the fine details, and the GOM system can resolve most of the fine details but the 3D features are less sharp (probably due to inherent filtering); 2) even though our low-resolution system does not show sharp details, it captured most of the important features; and 3) GOM system discarded numerous data points, creating holes on the surface. The white areas (i.e., holes) in Figure 3.7(b) indicated missing data points from the GOM system. These points were discarded for reasons we could not find out for sure. They could be regarded as bad quality points due to shadows, reflections, occlusions, or others.

A region of dark shoe bottom, shown in Figure 3.7(a), was also measured. Figure 3.7(b)-(d) show corresponding rendered images with MeshLab. All three systems captured the trademark of the shoe. The high-resolution and the GOM system captured the grid intent in the ellipse shape region. The dot feature all over the shoe bottom is also captured sharply

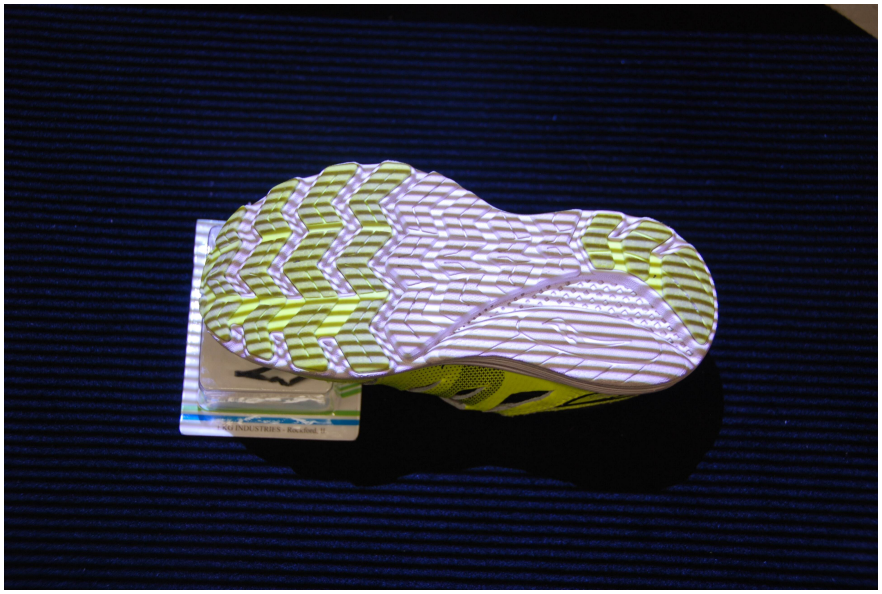

**Figure 3.5.** The light shoe bottom while being measured.

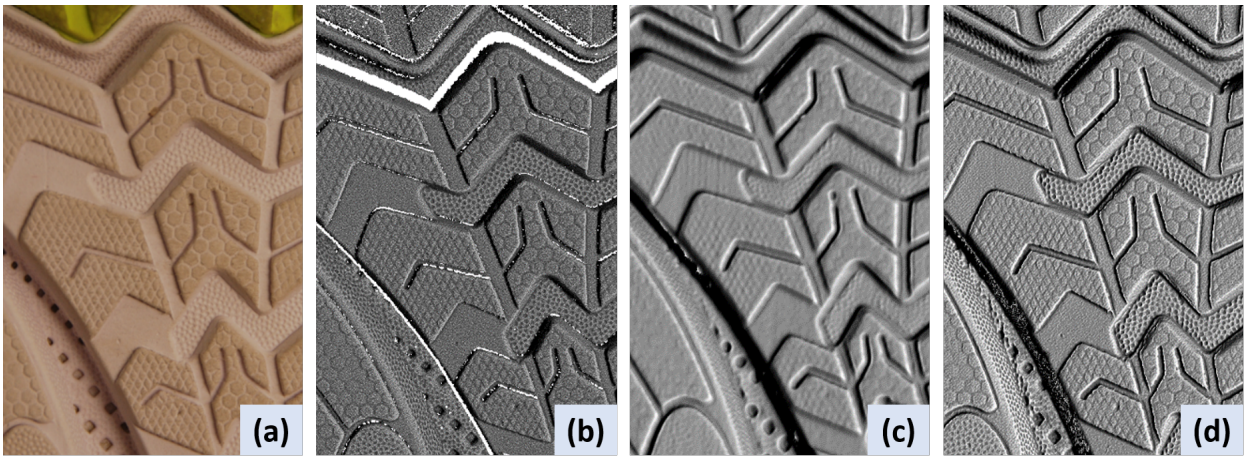


**Figure 3.6.** Measurement results of a region of light shoe bottom. (a) 2D photograph (b) 3D captured by GOM system; (c) 3D captured by our low-resolution system; (d) 3D captured by our high-resolution system. (b)-(d) rendering results with MeshLab.

by the high-resolution system. The three similar observations for light shoe measurements hold for this test.

The dark shoe shown in Figure 3.9(a) was used to make impressions in three types of materials: Iowa sand (dried at ~140 ℃, sieved to pass through a No. 50 mesh sieve ~300 $\mu m$), Iowa soil (manually ground, sieved to pass through a No. 50 mesh sieve ~300 $\mu m$)

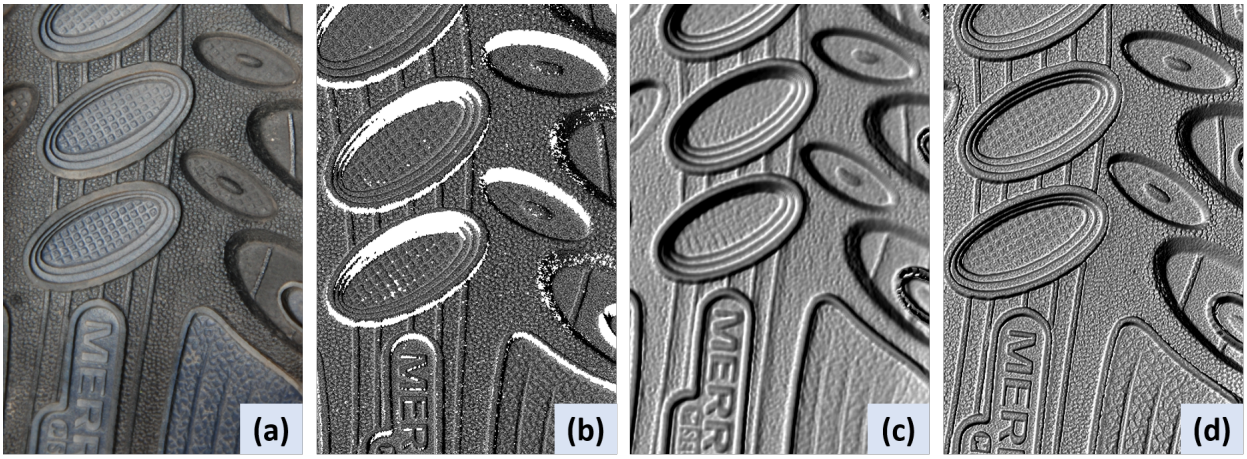


**Figure 3.7.** Measurement results of a region of dark shoe bottom. (a) 2D photograph (b) 3D captured by GOM system; (c) 3D captured by our low-resolution system (d) 3D captured by our high-resolution system. (b)-(d) rendering results with MeshLab.

and Iowa clay (dried at ~120 ℃, manually ground, sieved to pass through a No. 50 mesh sieve ~300 $\mu m$). The impressions are made by hand holding the shoe and press it into each material with a rolling motion mimicking a footstep scenario in which the heel strikes the ground first. Figure 3.8 shows the result of the impression made in a box containing Iowa Clay. Figure 3.9(b)-(d) shows photographs of prints made in each type of material. The red box outlines the area subjected to closer examination. Figure 3.9(e)-(h) show the corresponding regions with close examination. The clay preserves the detail of the shoe bottom the most, then soil, then sand, because it has the smallest grain size.

**Figure 3.8.** Impression made in a box containing the Iowa Clay.

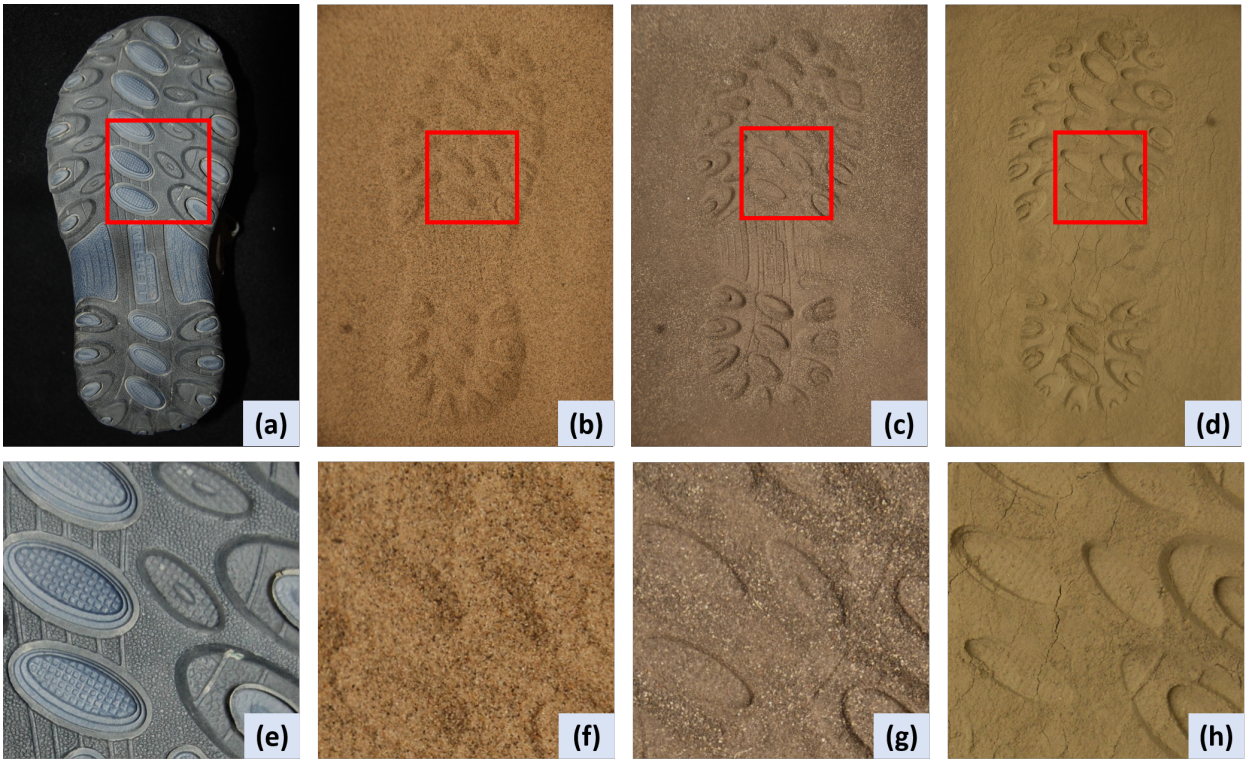


**Figure 3.9.** Impressions of the dark shoe in different materials. (a) Shoe; (b)Iowa sand; (c) Iowa soil; (d) Iowa clay; (e)-(h) the area of each respective image that was closely examined.

These impressions were measured by three systems and visualized in MeshLab. Figure 3.10 shows the rendering results. The results are quite impressive for prototype systems. It is obvious in the clay tests that the grid intents within the ellipse shape region of the shoe bottom are completely captured by our high-resolution system, even the low-resolution system captures the contour of the intents. The tiny cracks are also captured by our high-resolution system. For the sand impression, because of the larger grain size, we don't observe a huge difference between the three systems, but it demonstrates that our systems are able to capture every single grain of the sand. Our observations from these tests are: 1) our high-resolution system resolved all fine details, and the GOM system resolved most of the fine details but 3D features were less sharp; 2) our low-resolution system was not able to resolve some detailed features in Iowa soil and Iowa Clay, and 3) the GOM system had a lot missing data points (holes on the surface) that occurred with all other measurements.

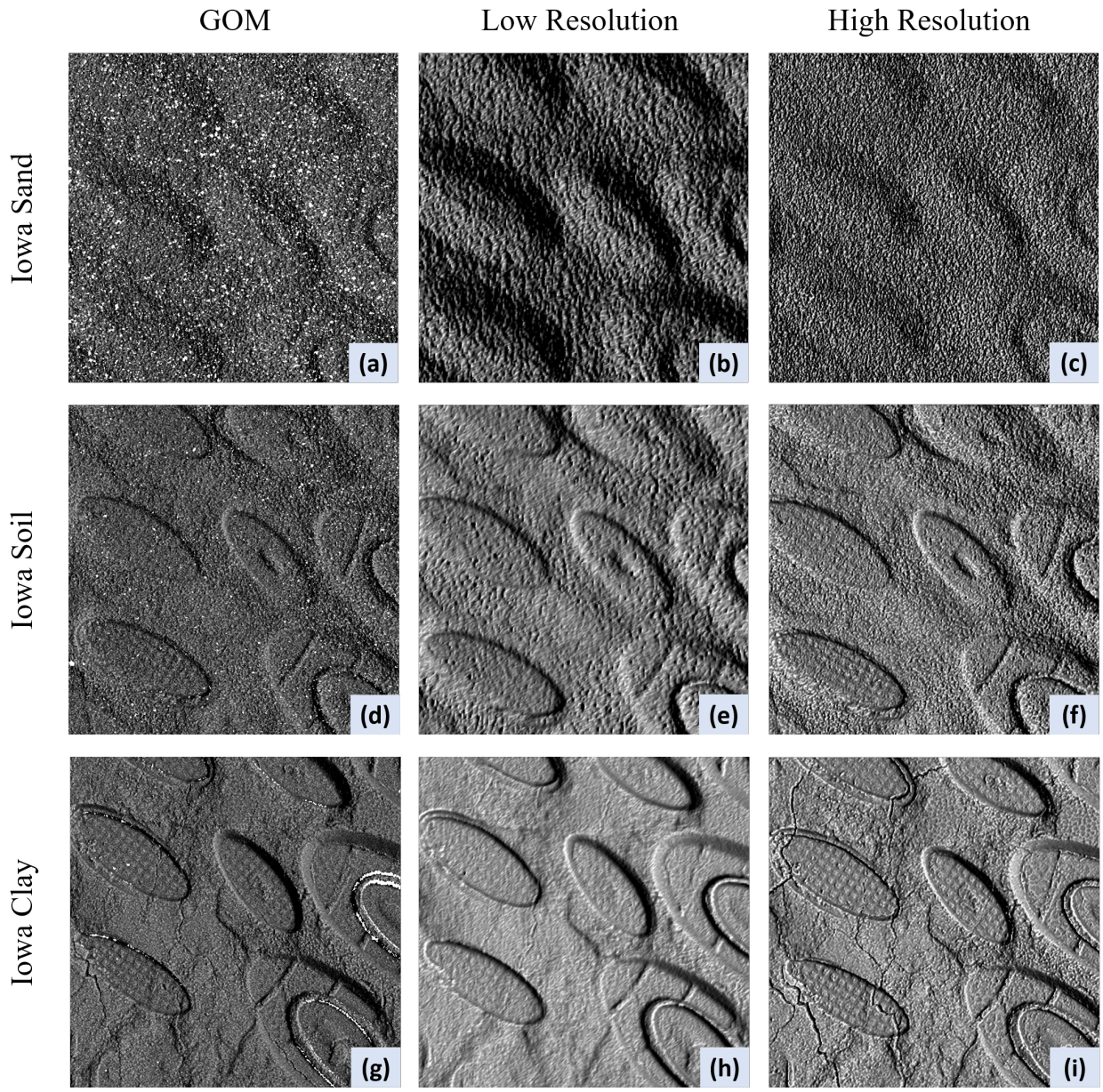


**Figure 3.10.** Measurement results of impressions in different materials made by the shoe shown in Fig. 8. Row 1: impression in Iowa sand; Row 2: impression in Iowa soil; Row 3: impression in Iowa clay. (a) impression captured by the GOM system; (b) impression captured by our low-resolution system with the Laplacian 1-step smooth offered by MeshLab; (c) impression captured by our high-resolution system with Laplacian 3-step smooth offered by MeshLab; (d) impression captured by the GOM system; (e) impression captured by our low-resolution system; (f) impression captured by our high-resolution system with Laplacian 1- step smooth offered by MeshLab; (g) impression captured by the GOM system; (h) impression captured by our low-resolution system; (i) impression captured by our high-resolution system with Laplacian 1-step smooth offered by MeshLab.

## 3.4 Evaluation of the color influence

The influence of object color on 3D measurement quality was evaluated by measuring a color sphere shown in Figure 3.11(a). The sphere was painted with three color bands, red (RUSTOLEUM Painter's touch satin poppy red), green (KRYLON Fusion satin spring grass), and blue (RUST-OLEUM Painter's touch satin ink blue). We specifically choose these paints that have satin texture because they dramatically reduce the light reflection. Figure 3.11(b)-(d) show 3D measurement results rendered with MeshLab. Our observations from this test are: 1) the GOM system produced fewer data points for the red and green areas than the blue area, which might be the result of using blue structured light so that when the GOM system is trying to find the optimal exposure time for the blue area, the red and green areas are underexposed; 2) our systems were less influenced by surface color than the GOM system; 3) although we have already tried to minimize the reflection, the GOM system failed to produce measurements and created two circular holes in the middle, a problem not observed with our systems.

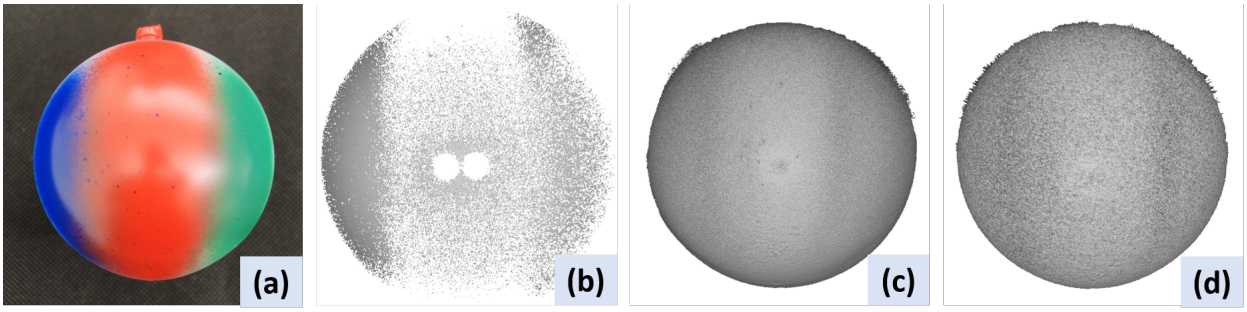


**Figure 3.11.** Measurement results of a colorful sphere. (a) 2D photo; (b) 3D captured by the GOM system; (c) 3D captured by our low-resolution system; (d) 3D captured by our high-resolution system.

## 3.5 Summary of Comparisons of GOM and Low- and High-Resolution System Results

While the GOM was selected for these experiments as a widely recognized high-quality 3D imaging system, our comparisons are limited by a number of factors that are inherent to that system and beyond our control. There are internal filtering and pixel removal algorithms

being used in this commercial system that undoubtedly are addressing understandable noise and high spatial error artifacts. Indeed, we encounter noise sources in the data with our systems as well. The thresholds for filtering and pixel removal in the commercial system are not particularly accessible or customizable by the casual user and undoubtedly affect the density, uniformity, and noise levels in the reported data. We have chosen a different approach to spatial noise with the spatial smoothing described in this publication. Our choice of methods and filter parameters results in no loss in density or uniformity of data and retention of good spatial detail that for the high-resolution system matches or exceeds the accuracy of the GOM system. We believe that this combination of data density, uniformity, and accuracy are all important for forensic documentation of samples and impressions. Therefore, we believe that this approach is the correct approach for dealing with spatial error in 3D imaging for forensic applications.

In all of our head to head comparisons, the GOM system produced accuracy comparable or slightly poorer than our high-resolution system with noticeable point loss, that can be exacerbated by blue-colored samples. The low-resolution system has accuracy approximately a factor of two worse than the high-resolution and the GOM systems, but it has a significant increase in area coverage. In cases where a larger area of coverage is required, a low-resolution system (or a dual resolution system with two cameras) may be preferable.

### 3.6 Technical Details of Low- and High-Resolution Systems

The DFP technique and phase-shifting-based fringe analysis technique were employed by both systems. The binary defocusing technique was employed because it eases the stringent requirement of precise timing control and makes the system immune to the projector's non-linear response. Furthermore, the binary defocusing allows the flexible exposure time choice that enables the auto-exposure algorithm and leads to the development of HDR algorithm [37].

The hardware system was designed to be portable and easy to set up, and the software GUI was developed to be intuitive to operate with minimal training. The resolution for the projector employed in both systems is $912 \times 1140$ pixels. The low-resolution system uses one $1920 \times 1200$ pixels CMOS camera and a 16 mm lens which achieves approximately

137 dpi with a field of view (FOV) of 14" × 8.75" (355.6mm × 222.25mm). The high-resolution system uses one 2048 × 1536 pixels CMOS camera and a 25 mm lens which achieves approximately 400 dpi with a FOV of 5.12" × 3.84" (130.05mm × 97.54mm). The distance between the low- and high-resolution systems and the measured object was designed to be 0.5 m.

We understood that the FOV of our high-resolution system cannot cover the entire shoeprint in one capture. This is a problem that we are working on for the second phase of research. We will develop new algorithms that can stitch multiple scans easily with minimum user inputs.

The projector projects binary patterns sequentially at 60 Hz onto the object surface and the camera captures the scattered patterns by the object at the same speed. To reconstruct each 3D shape, 18 phase-shifted binary patterns with a fringe period of 18 pixels and 6 gray-coded patterns are required. The software algorithm analyzes the phase-shifted fringe patterns to extract the wrapped phase map (a phase map with $2\pi$ discontinuities), and further unwrap the phase using the 6 gray-coded patterns. The unwrapped phase was further used to reconstruct 3D shape based on the calibration parameters of the system. It takes approximately 0.5 seconds to the system to acquire necessary images for each 3D scan, and approximately 2 seconds on a Laptop (Lenovo T480) to process 3D data. If HDR option is elected, it takes approximately 8 seconds to finish the measurement. Our software GUI allows a user to save data with or without filtering.

The rms error of planar surface measurement is approximately $0.05\,mm$ (790268 data points) for the low-resolution system with a measurement area of $200 \times 160\,mm^2$ and $0.027\,mm$ (1697702 data points) for the high-resolution system with a measurement area of $100 \times 80\,mm^2$. The rms measurement error of a sphere with a diameter of $80\,mm$ is $0.125\,mm$ (97978 data points) for the low-resolution system, and $0.070\,mm$ (822864 data points) for the high-resolution system. Both systems are not strongly influenced by the color of the object surface.

## 3.7 Lab Tests Comparing Scans to Traditional Collection Techniques

To compare our 3D imaging technology with traditional impression evidence collection techniques using evidence quality photography and conventional casting methods, our prototype systems are sent to the forensic scientist on our team, Mr. James Wolfe, to perform evaluations. The experiments captured shoe or tire impressions in commonly encountered substrates, clay (grain size $< 0.01$ mm), damp sand (grain size $< 1$ mm), dry fine sand (grain size 0.2-0.6 mm), damp fine silt (grain size $< 0.1$ mm), wet snow (air temperature 1 °C), and dry snow (air temperature -8 °C).

The impression in each experiment was documented by digital 2D photography using oblique lighting, scanned with the 3D scanners, and then cast. Dental stone (Buff Labstone, Garreco Inc.) was used to cast the clay, sand, and silt impressions, and snowprint plaster (SnowStone, Evident Inc.) was used to cast the snow impressions. To produce a 3D "digital cast" the captured 3D image was rotated to view the backside of the scan. This digital cast was then compared to the physical cast, photograph, and source shoe or tire. The 2D photograph was flipped horizontally to correspond to the casts and source shoe or tire.

### 3.7.1 USPA test shoe for impressions in clay

Figure 3.12(a) shows the USPA shoe outsole used to create impressions in clay. We intentionally create cut marks with different sizes and a couple of rockholds in order to evaluate the performance of each documentation method. Figure 3.12(b) shows the region that was closely examined for this study. Figure 3.12(c)-(d) respectively show 3D data captured by our low-resolution and high-resolution system for the shoe. In this case, all 3 methods resolve all the cut marks and rockholds. However, the higher resolution system clearly shows sharper details and resolves smaller features better.

### 3.7.2 USPA Test Impression in Clay (Grain Size $< 0.01$ mm)

The USPA shoe above was used to make an impression in clay. Figure 3.13(a) shows the evidence quality photograph. The impression was then captured by our high-resolution and

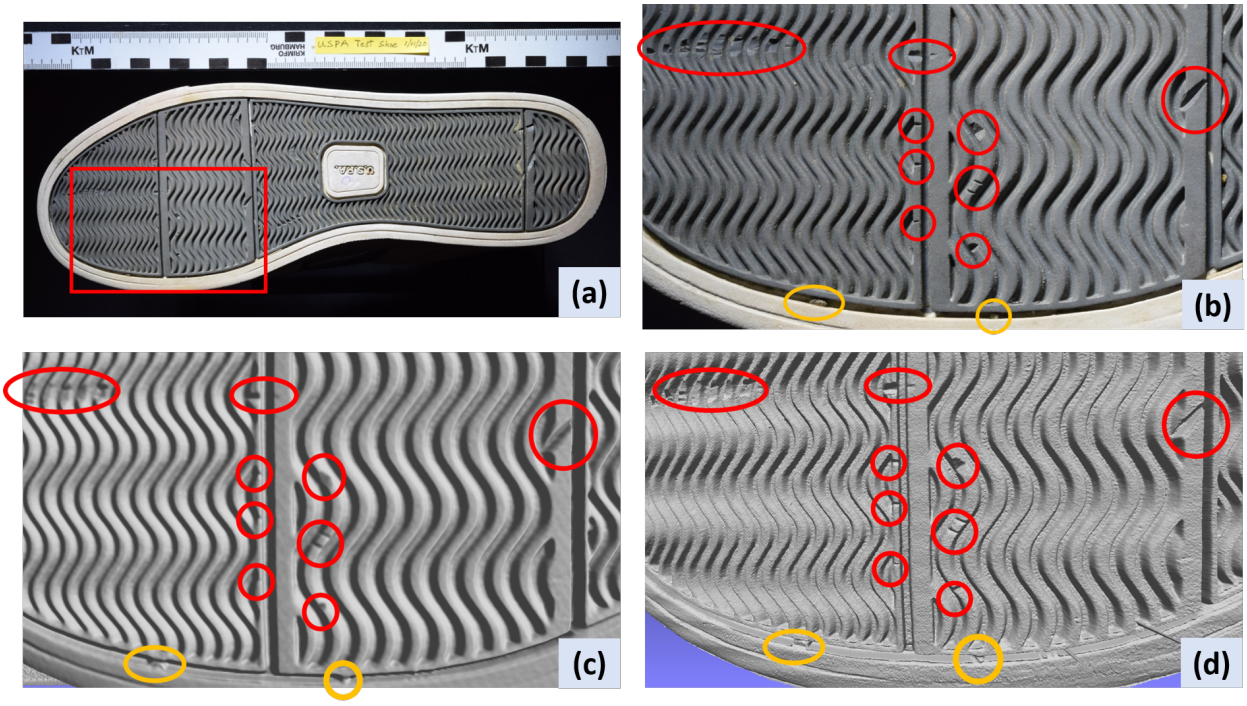


**Figure 3.12.** The USPA shoe used to create the clay impression. The red box outlines areas with cut marks and rockholds subjected to closer examination. The red circles outline the cut marks and the orange circles outline two small rockholds. (a) 2D photograph; (b) region that was closely examined; (c) low-resolution 3D scan; (d) high-resolution 3D scan.

low-resolution systems, as well as the physical cast. From the captured 3D data, we rotated the scan to view the backside creating a "digital cast." Figure 3.13(b)-(d) show the results.

As in the results of system resolution evaluation, the cut marks and rockholds is not a problem for our high-resolution system. Our observations from this test are: 1) the evidence quality photograph with oblique lighting resolved all 10 test cuts and the two small rockholds, but the lack of 3D information would make it difficult to characterize the small rockholds; 2) the cast resolved all 10 test cuts and both small rockholds, yet small bubbles in the casts (casting artifacts) interfered with characterizing several of the test cuts and also had the potential to obscure other impression detail; 3) our low-resolution 3D scan clearly resolved 9 of 10 test cuts and also the two small rockholds, the smallest test cut could be barely visualized using virtual oblique lighting in MeshLab; 4) our high-resolution 3D scan clearly

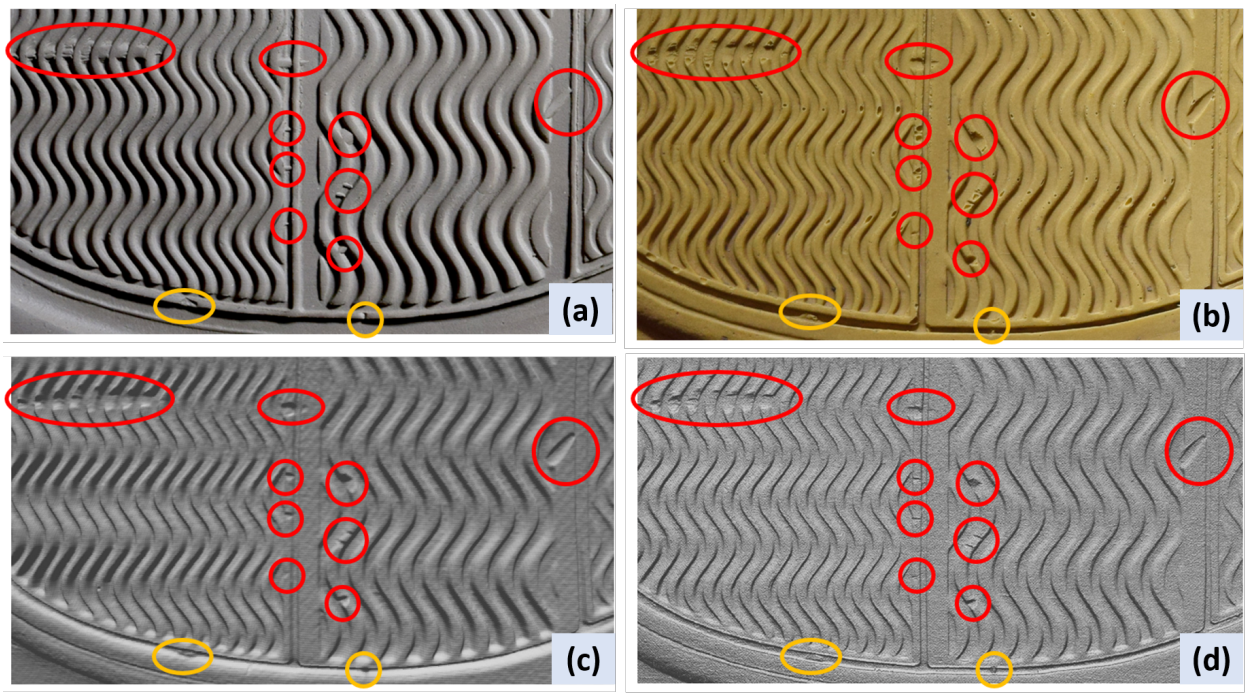


**Figure 3.13.** Test of shoe impression in clay. The red circles outline locations that correspond to test cuts in the shoe outsole and the orange circles outline locations that correspond to small rockholds in the shoe outsole. (a) Evidence quality 2D photograph: resolved 10 test cuts and the two small rockholds; (b) photograph of the conventional physical cast: resolved two small rockholds and all 10 test cuts, but the small bubbles produced in the casting process made visualization difficult for several of the cuts; (c) low-resolution 3D digital cast: resolved 9 out of the 10 test cuts, and two small rockholds; (d) high-resolution 3D digital cast: resolved all 10 test cuts and two small rockholds

resolved all 10 test cuts and the two small rockholds. The high-resolution scan also provided sharper detail of the outsole design and test cuts, compared to the low-resolution scan.

### 3.7.3 USPA Test Shoe for Impressions in Damp Sand and Damp Fine Silt

Figure 3.14(a) shows the USPA shoe outsole used to create impressions in damp sand and damp fine silt. This is the same shoe used for the clay test, however, these tests were performed at an earlier date and only one rockhold was characterized. Figure 3.14(b) shows the region that was closely examined for this study. Figure 3.14(c) and Figure 3.14(d) respectively show 3D data captured by our low-resolution and high-resolution system for

the shoe. The higher resolution system clearly shows sharper details and resolves smaller features better.

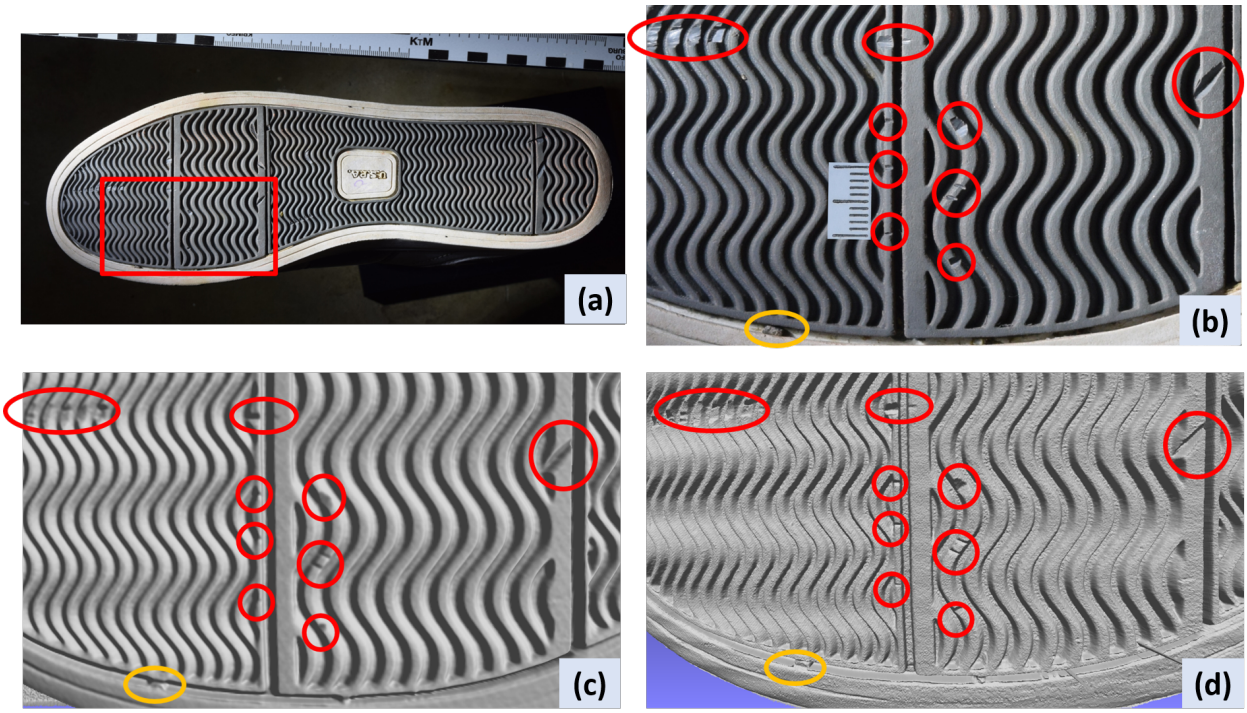


**Figure 3.14.** The same USPA shoe as Figure 3.12 used to create impressions for examination. The red box outlines area with cut marks and rockhold subjected to closer examination. The red circles outline the cut marks and the orange circle outlines the small rockhold. (a) 2D photograph; (b) region that was closely examined; (c) low-resolution 3D scan; (d) high-resolution 3D scan.

### 3.7.4 USPA Test Impression in Damp Sand (Grain Size $<$ 1 mm)

The USPA shoe was used to make an impression in damp sand. Figure 3.15 shows the corresponding results. Our observations from this test are: 1) both low- and high-resolution 3D digital casts resolve the test cuts almost as well as the photograph; 2) the rockhold was difficult to characterize in the 2D photograph; 3) compared to the physical cast, 3D digital casts captured more details; 4) because the sand has a larger grain size and it is more fragile, there are pouring artifacts present on the physical cast, destroying some areas of details.

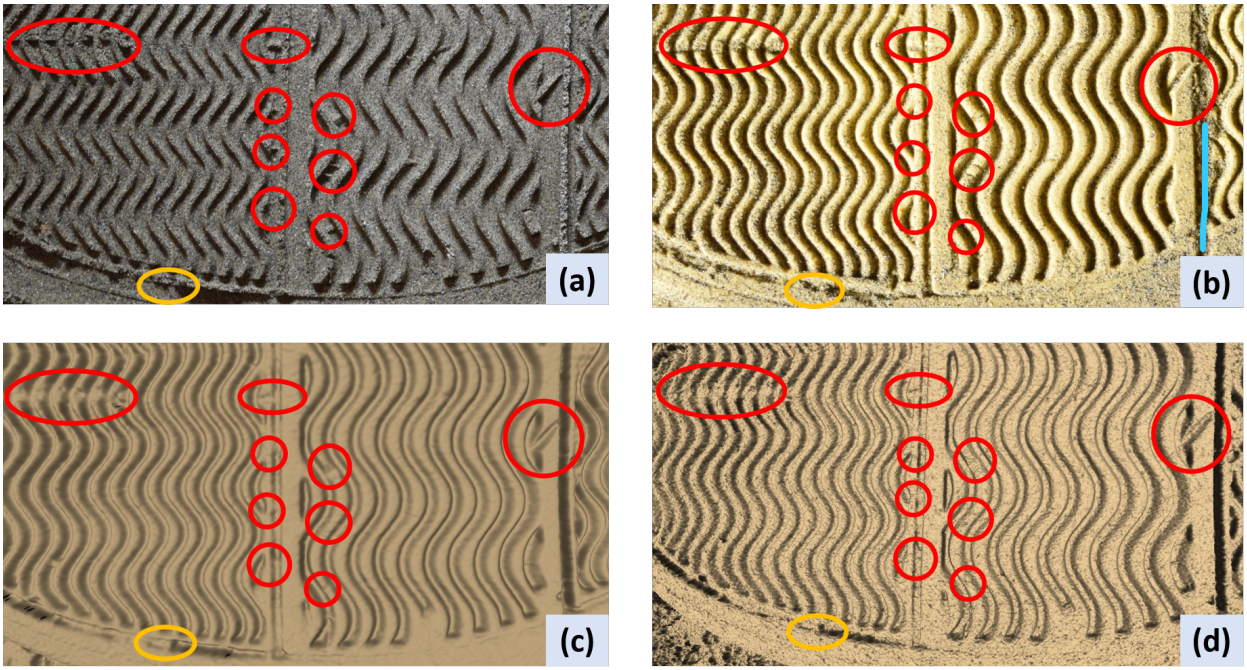


**Figure 3.15.** Test of shoe impression in damp sand. The red circles outline locations that correspond to test cuts in the shoe outsole, the orange circle outlines the location that corresponds to the small rockhold in the shoe outsole, and the blue curve highlights the pouring artifacts. (a) Evidence quality 2D photograph: resolved 7 of 10 test cuts, the small rockhold is not clearly visible; (b) conventional physical cast: resolved 5 out of the 10 test cuts, partially resolved the small rockhold; (c)low-resolution 3D digital cast: resolved 5 out of the 10 test cuts, partially resolved the small rockhold; (d) high-resolution 3D digital cast: resolved 6 out of the 10 test cuts, partially resolved the small rockhold.

### 3.7.5 USPA Test Impression in Damp Fine Silt (Grain Size <0.1mm)

The same USPA shoe was used to make an impression in damp fine silt. Figure 3.16 shows the corresponding results. Our observations are: 1) all methods resolved the 10 test cuts; 2) because the damp fine silt used has a much smaller grain size than the sand, the 3D digital casts have better results than the previous test; and 3) like the previous test, the conventional cast has the worst performance, with some features eroded or more rounded because the impression was degraded by the cast.

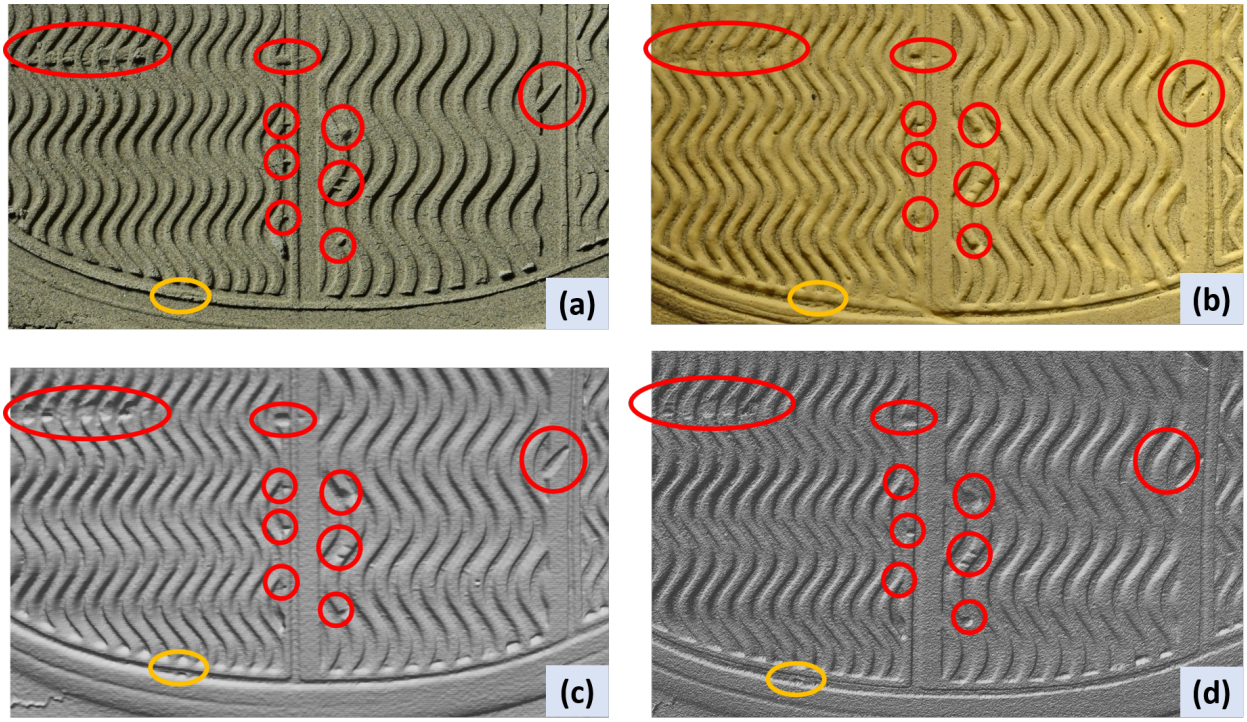


**Figure 3.16.** Test of shoe impression in damp fine silt. The red circles outline locations that correspond to test cuts in the shoe outsole and the orange circle outlines the location that corresponds to a small rockhold in the shoe outsole. (a) evidence quality 2D photograph resolved all 10 test cuts but did not resolve small rockhold; (b) conventional physical cast: resolved 9 of 10 test cuts but did not resolve small rockhold; (c) low-resolution 3D digital cast: resolved all 10 test cuts and small rockhold; (d) high-resolution 3D digital cast: resolved all 10 test cuts and small rockhold.

### 3.7.6 Tire impression in dry snow (air temperature -8°C)

The system was further evaluated by capturing impressions in snow. Figure 3.17 shows the tire (Studded Nokian Hakkepilitta 7SUV 265/70R16 winter tire) that was used to create the impression in dry (air temperature -8°C) snow. Figure 3.18 shows the visual results. Our observations from this test are: 1) the limited quality of the impression seems to make the high and low-resolution scans equal in visualizing detail; 2) the low-resolution scan rendering provides a little more contrast making it easier to discern the studs and rockholds; and 3) 3D scans resolved comparable detail to the physical cast. It is important to note that from our experience, spray painting an impression in dry snow did not make a noticeable difference in our scanned data quality.

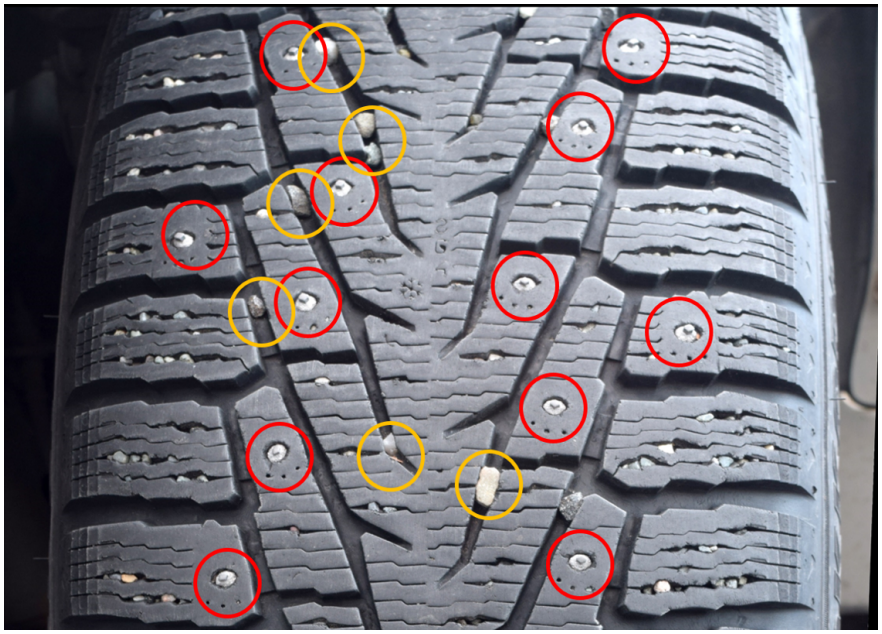

**Figure 3.17.** Two-dimensional photograph of the tire (Studded Nokian Hakkepilitta 7SUV 265/70R16) used to make the impression in dry (air temperature -8°C) snow. The red circles outline the area with tire studs and the orange circles outline the larger rockholds in grooves.

### 3.7.7 XtraTuf Test Impression in Wet Snow (air temperature 1°C)

A shoe impression in wet snow (air temperature 1°C) was also tested. We found that the wet snow causes a strong reflection problem and coating the impression with gray spray paint (KRYLON Colormaster Primer gray) was necessary before 3D capture. Furthermore, under sunlight, the light-blocking skirt is needed to block the bright ambient light for a good quality scan. Figure 3.19 shows the shoe (XtraTuf) that was used to make the impression and the outsole region that was closely examined.

Figure 3.20 and Figure 3.21 show the results. Our observations from this test are: 1) the 2D photograph resolved the worn areas, barely allowed the visualization of the patent label, and had difficulty resolving the rockhold; 2) since the impression is quite deep, it was difficult to capture high-quality 2D photographs due to shadowing of the oblique light; 3) the physical cast resolved the rockhold and the worn areas, but portions of the outsole design in the heel were melted by the casting process, shown in figure 3.21; 4) with the help of the gray primer spray paint and the light-blocking skirt, 3D digital casts clearly resolved the

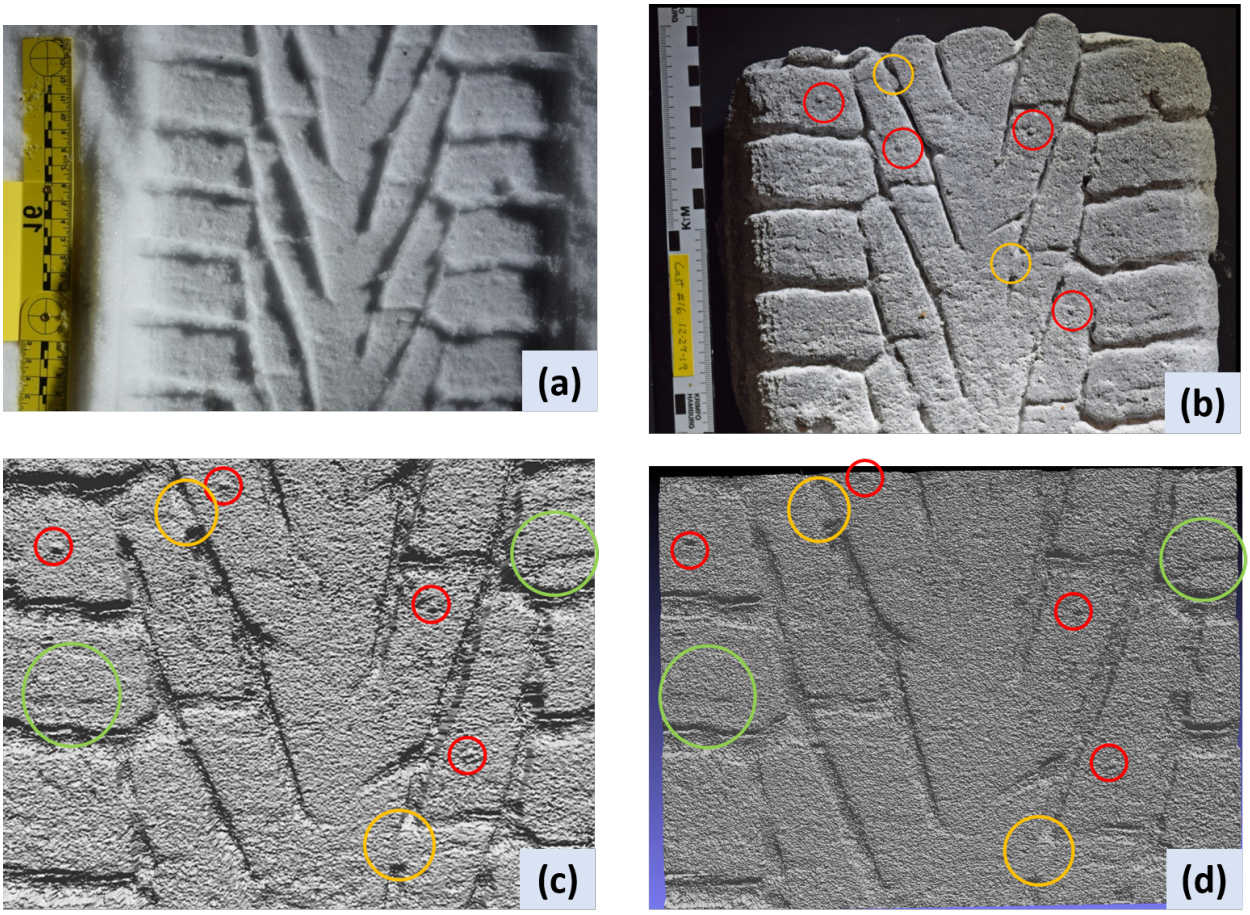


**Figure 3.18.** Test of tire impression on dry snow (air temperature -8°C). The red circles outline the areas with tire studs, the orange circles outline the larger rockholds in grooves, and the green circles outline the sipes widened by the smaller rockholds enough to be partially visualized in the impression. (a) Evidence quality 2D photograph; (b) conventional physical cast; (c) low-resolution 3D digital cast; (d) high-resolution 3D digital cast.

worn areas and the rockhold. The ability to view the digital cast from different angles gives 3D scanning the advantage of interpreting the worn areas; 5) the patent label is much more obvious in 3D digital casts.

### 3.7.8 Tire Test Impression in Fine Dry Sand (Grain Size 0.2-0.6 mm)

We tested a tire impression in fine dry sand (0.2-0.6 mm). Figure 3.22 shows the tire we used (Michelin X LT 265 70R16) and its corresponding 3D scan. Our observations from this test are: 1) the evidence quality photograph clearly resolved all 4 wear bars but was only

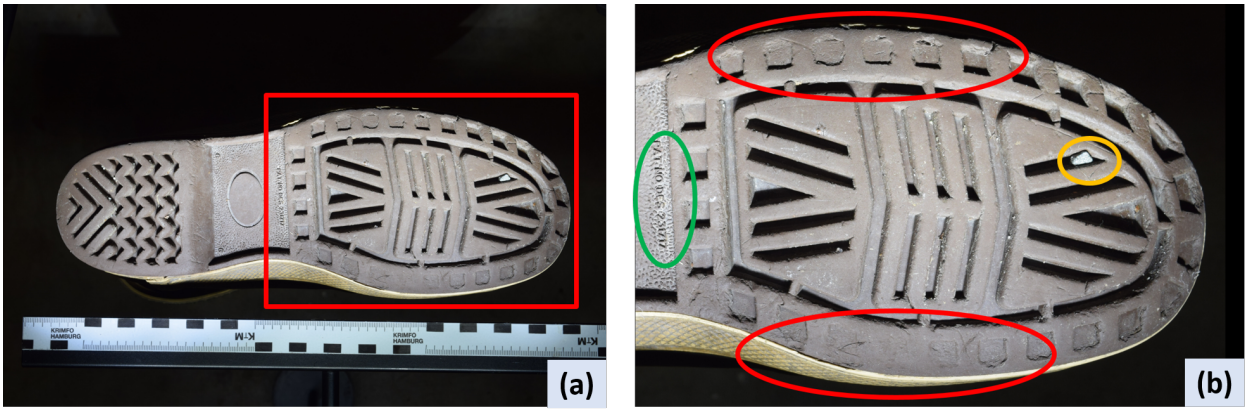


**Figure 3.19.** 2D photographs of the shoe (XtraTuf) used to create the impression on wet (air temperature 1°C) snow. The red box outlines the area with cut marks and rockhold that was subjected to closer examination. The red circles outline the areas of extreme wear, the orange circle outlines the rockhold and the green circles outline the patent label. (a) photograph of the shoe bottom; (b) close-up photograph of the front portion of the shoe.

able to discern 2 of 4 rockholds. It did not have 3D information to easily characterize the rockholds; 2) the physical cast destroyed much of the fine impression detail either due to fragile soil or by casting artifacts, only one wear bar was clearly visualized and no rockholds were clearly visible, and only small portions of the mold flash were apparent; and 3) our low-resolution 3D digital cast was able to resolve all 4 wear bars and 3 out of 5 rockholds in a larger area scan, clearly resolved the mold flash, and 3D information helped to characterize the rockholds.

## 3.8 Tire Imaging for Known Sample Comparison to Impressions

As part of this study, our team has developed a system for imaging tire treads using the same low-resolution imaging system evaluated for imaging tire impressions. The intent is to allow examiners to capture both 3D images of impressions and of tire treads under weight-loaded conditions to support computer-aided comparison visualization and potentially providing data for computer-based searching and comparison tools. The system images the tire tread through a transparent platen with calibrated hydraulic force applied. While a working and affordable system has been developed, it has not been quantitatively

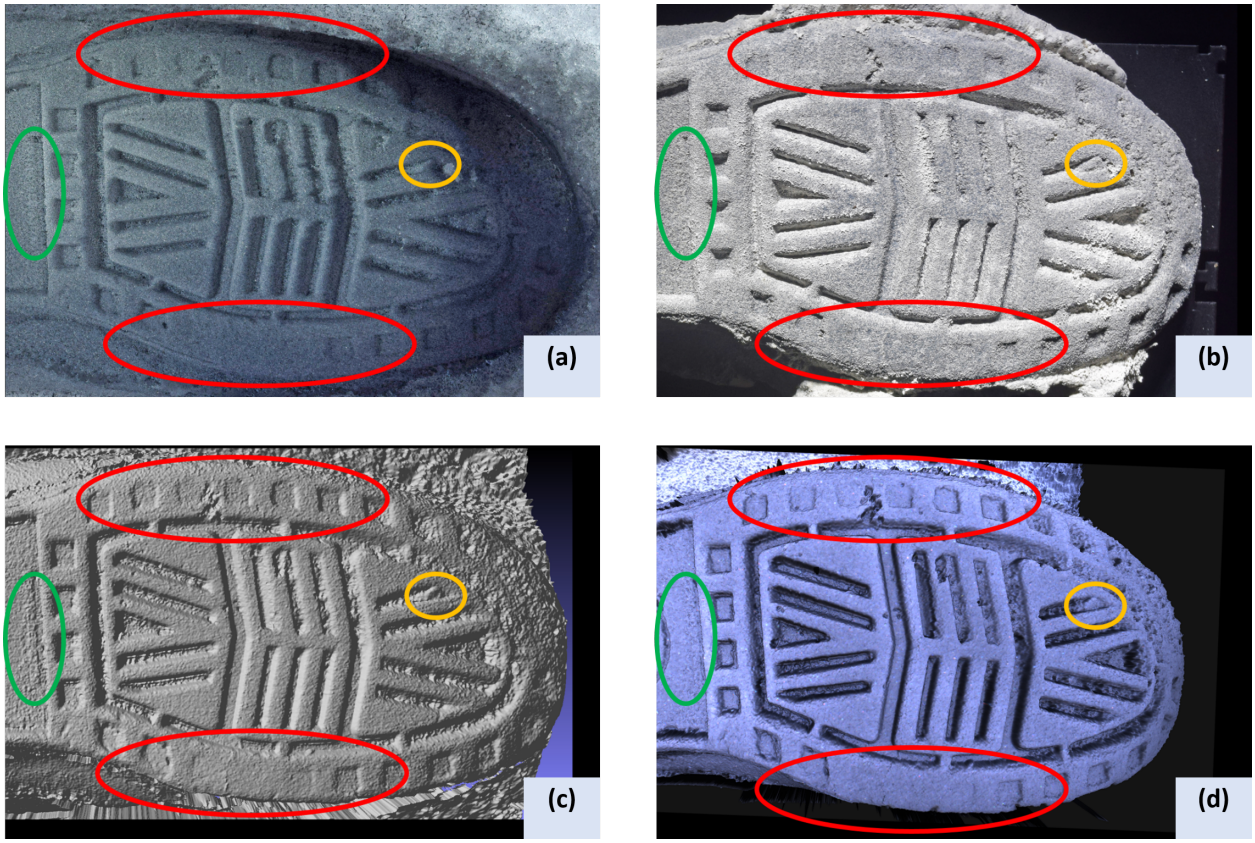


**Figure 3.20.** Test of shoe impression in wet snow (air temperature 1°C). The red circles outline the areas of extreme wear, the orange circles outline the rockhold and the green circles outline the patent label. (a) Evidence quality 2D photograph; (b) conventional physical cast; (c) low-resolution 3D digital cast rendered with MeshLab; (d) low-resolution 3D digital cast rendered with our own 3D viewer in textured mode.

evaluated for any of these applications and so we are not including details about this system in this publication. However, it will be available for future development and evaluation in follow-on work.

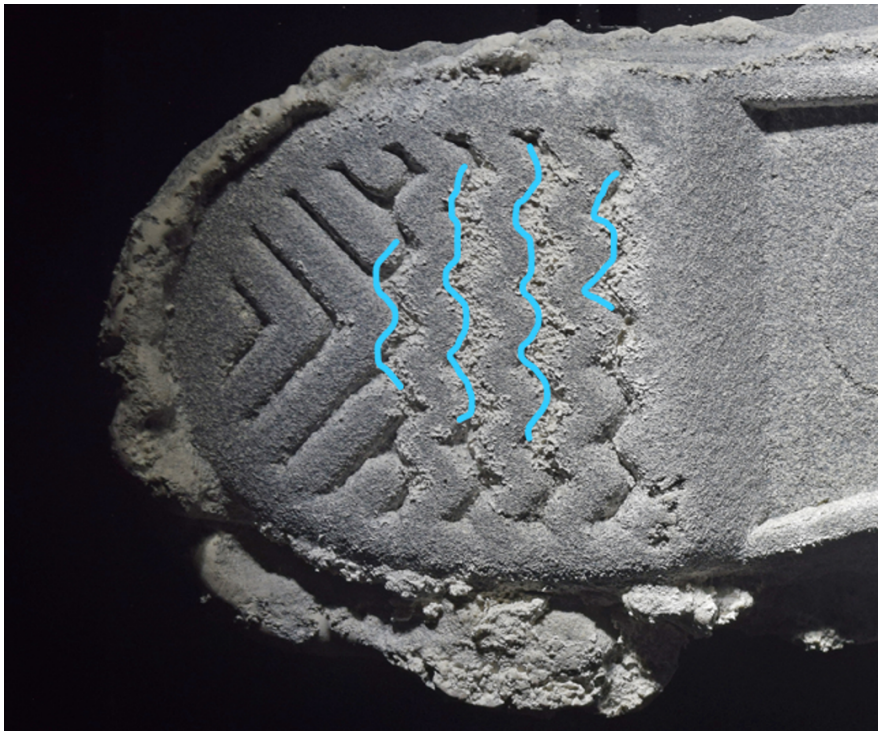

**Figure 3.21.** Conventional physical cast of the heel of the shoe impression in wet snow (air temperature 1°C). Blue lines indicate areas of impression that were degraded/melted during the casting process.

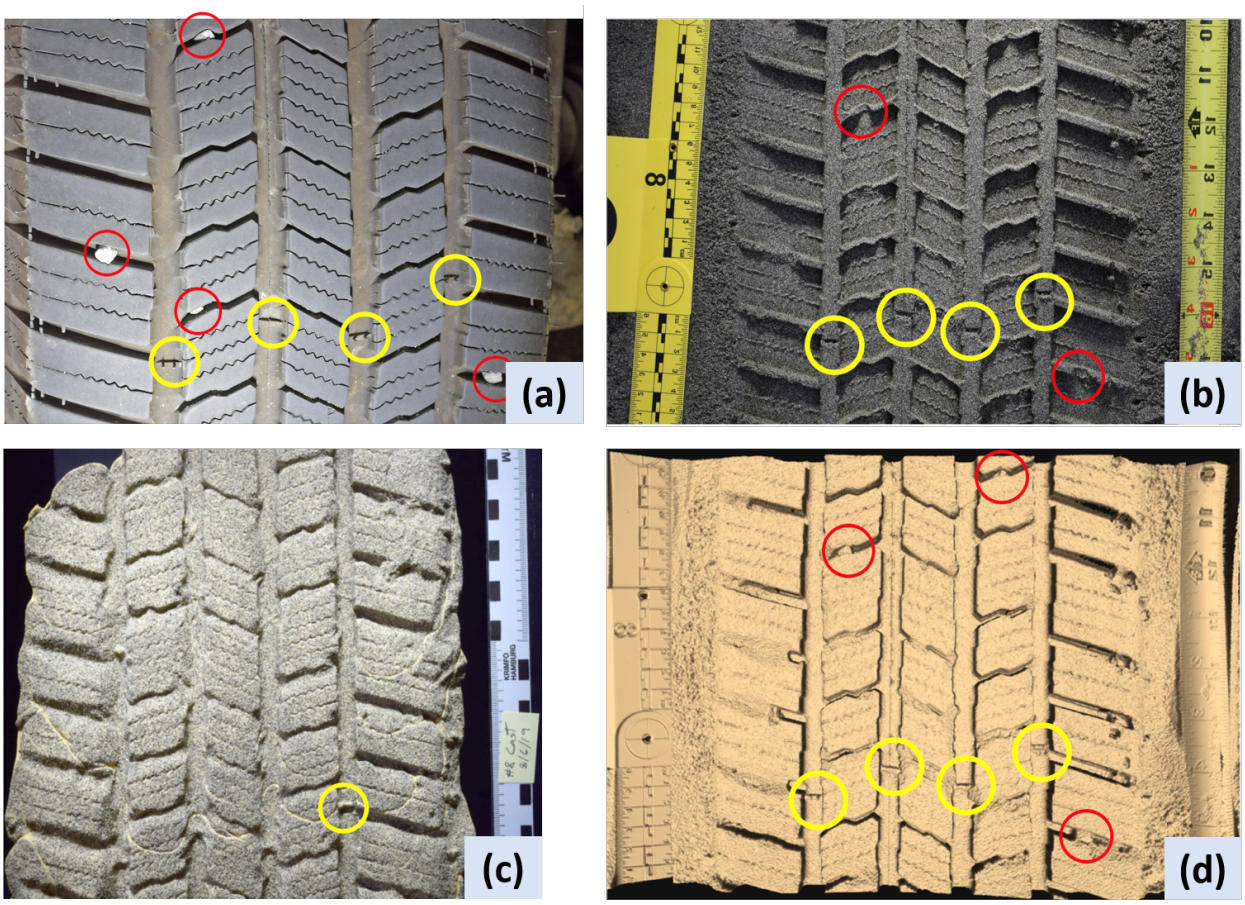


**Figure 3.22.** Test of tire impression in dry sand. (a) Photograph of the tire used to make the impression. Red circles outline the rockholds, and yellow circles outline the wear bars molded into the tire grooves; (b) evidence quality 2D photograph resolved 2 out of 4 rockholds and 4 out of 4 wear bars; (c) conventional physical cast: resolved 1 out of 4 wear bars, and 0 out of 4 rockholds; (d) low-resolution 3D digital cast: resolved 3 out of 5 rockholds and 4 out of 4 wear bars.

# 4. SUMMARY

This thesis presents a novel noninvasive optical 3D imaging sensor that can capture critical and detailed characteristics of footwear and tire impressions in various substrates and uneven surfaces that require forensic examinations. Two prototype systems were developed. Both systems use DFP technique to project fringe patterns onto the measuring surface and then apply the phase-shifting algorithm and gray coding phase unwrapping to retrieve the phase information. Finally, the 3D models are recovered with the pinhole camera model assumption. There is one 2048 $\times$1536 pixels resolution CMOS camera and one 912 $\times$1140 pixels resolution projector on the high-resolution system. There is one 1920 $\times$1200 pixels resolution CMOS camera and one 912 $\times$1140 projector pixels resolution on the low-resolution system. For accuracy evaluation, the RMS error of the planar surface measurement is 0.05mm and 0.027mm for the low and high-resolution system. The RMS error of a sphere with a diameter of 80mm is 0.125mm and 0.07mm for the low and high-resolution system. For resolution inspection, both prototype systems measure shoe bottoms and shoe impressions in various substrates. The results have shown to be very impressive that they successfully capture the fine details of the objects. Last but not least, the white light used in our DFP technique has proven to be making our prototype systems more immune to the color of the measuring object. The total cost of the system is approximately $3000 USD. We compared all of the performance of our two prototype systems with the commercially available high-end 3D scanner (GOM ATOS Core, Germany, > $30000 USD) and it shows that our high-resolution system achieves similar or sometimes better results than the GOM system. Overall, they have the merits of being 1) more affordable (a fractional cost of the commercial system); 2) much easier to operate; and 3) more robust.

The prototype systems are then sent to the forensic scientist, Mr. James Wolfe, for lab tests. The systems are used to capture shoe and tire impressions in clay, dry sand, damp sand, damp fine silt, dry snow, and wet snow. In almost every situation, the 3D imaging technique outperforms the 2D photograph and physical casting. Our technology demonstrates its superiority because it 1) is non-destructive; 2) collects more evidence detail than casts, especially when an impression is fragile (e.g. in dry fine sand); 3) it saves time

and costs less to collect each impression; 4) results in a digital file that can easily be shared with other examiners. The digital impression captured at the crime scene allows analysts in the lab to view a digital impression like they were studying the actual impression in situ. The scan also provides a 3D "digital cast" that represents the actual shoe or tire that produced the impression. The ability to view the digital cast from different angles gives 3D scanning the advantage. Overall, the 3D digital cast provides detail equal to or better than that of a physical cast and is invaluable not only for comparison purposes but also as an investigative aid. Therefore, this technology promises to be transformative to the field as it allows the fast, shareable collection of 3D detail of impressions with minimal training.

# 5. FUTURE WORK

The work that has been done in this thesis has demonstrated the potential and the ability of our systems to be used in a true crime scene. However, there are still several improvements that can be explored before deploying these technologies into the field.

Our low-resolution system captures a large area with 137 dpi and our high-resolution system capture a smaller area with 400 dpi. From our experiments, we found that when capturing impressions from some substrates that have coarser grain size or poorer quality, such as sand and snow, the low-resolution system is adequate to acquire most of the details and replace the physical cast. In this situation, the low-resolution system is preferred over the high-resolution system because it can capture a larger area. While when capturing impressions or object that has finer details like shoe bottom or impressions in clay, the high-resolution system has to be used in order to recover those delicate features. Thus, both systems are required in a crime scene. This can be addressed with 3 options. First, create a high-resolution system with a large field of view. Second, bring both low and high-resolution systems to the field. Third, incorporate high and low-resolution cameras into one dual resolution system. The first option will not be acceptable by most of the forensic agencies because using an even higher resolution camera will increase the cost significantly. The second option is also not preferred since bringing two systems to the site will be cumbersome. The last option will be the most viable option because it only increases a moderate cost while maintaining the merits of both high and low-resolution systems. Therefore, one of the future works will be creating a dual-resolution 3D imaging device that could capture the impression with high and low resolution simultaneously.

Even with the dual resolution system, the field of view of the high-resolution camera is still not enough to cover a whole tire track or shoe impression. So, software that can stitch multiple scans together has to be developed alongside. Usually, the stitching process is done by the following procedures. Manually align the scans by selecting corresponding feature points from each scan, use iterative closest point algorithm (ICP) to refine the alignment, then merge the 3D mesh with surface merging algorithms. With the dual resolution, we can also use the low-resolution scan to aid high-resolution stitching. Further, We will investigate

artificial intelligence algorithms that can align the scans automatically with minimum human input. Another important part regarding software development is its ability to be able to manipulate the virtual lightings on the 3D model. In real life, the 2D evidence photographs have to be taken under various oblique lightings in order to minimize any occlusion issue. In the virtual world, one can simply take a 3D scanning model and manipulate the virtual lighting to recognize every detail on the model. The software is expected to be capable of exporting 2D photographs with desire resolutions and achieve similar or higher quality than traditional 2D photographs.

The system also has to go through more comprehensive experiments. In this research, the systems only capture footwear and tire impressions in sand, silt, clay, and snow. In the future, the experiments will include other types of soil with different textures and grain sizes, such as humus or loam. The substrates will also be in various moisture conditions from dry to saturate. More tests in all types of snow are required as well, as the snow is one of the most challenging materials to capture. The experiments will be conducted in different lightings, including dark, overcast, sunlight to dazzlingly bright. Additional models of shoes and tires will be used to make impressions. As always, all the experiment results will be compared with 2D evidence quality photographs, physical casts, and the results from the commercial high-end 3D scanner. Evaluation of the user experience will keep on going by introducing and sending our systems to the forensic community. If possible, we would like to apply our systems to a true crime case like what the other research has done. Nothing is more valuable than the feedback from the front line investigator. Although it seems like there are still lots to be done before fully deploying this technology to forensic agencies, we are still excited about this work because we indeed see a bright future on it.

# REFERENCES


[1] M. Keglevic and R. Sablatnig, "Impress: Forensic footwear impression retrieval," in *Proceedings of the ARW & OAGM Workshop 2019*, 2019. DOI: 10.3217/978-3-85125-663-5-34.

[2] *Osac research needs assessment form*, 2016. [Online]. Available: https://www.nist.gov/system/files/documents/forensics/osac/SAC-Phy-Footwear-Tire-Sub-R-D-004-3D-Scanning_Revisions_Mar_2016.pdf.

[3] U. Buck, N. Albertini, S. Naether, and M. J. Thali, "3D documentation of footwear impressions and tyre tracks in snow with high resolution optical surface scanning," *Forensic Science International*, vol. 171, no. 2, pp. 157–164, 2007, ISSN: 0379-0738. DOI: https://doi.org/10.1016/j.forsciint.2006.11.001. [Online]. Available: http://www.sciencedirect.com/science/article/pii/S0379073806006712.

[4] *Forensic science technology working group operational requirements*, 2018. [Online]. Available: https://www.nij.gov/topics/forensics/documents/2018-11-forensic-twg-table.pdf.

[5] J. Geng, "Structured-light 3D surface imaging: A tutorial," *Adv. Opt. Photon.*, vol. 3, no. 2, pp. 128–160, Jun. 2011. DOI: 10.1364/AOP.3.000128. [Online]. Available: http://aop.osa.org/abstract.cfm?URI=aop-3-2-128.

[6] F. Ackermann, "Digital image correlation: Performance and potential application in photogrammetry," *The Photogrammetric Record*, vol. 11, no. 64, pp. 429–439, 1984. DOI: 10.1111/j.1477-9730.1984.tb00505.x. eprint: https://onlinelibrary.wiley.com/doi/pdf/10.1111/j.1477-9730.1984.tb00505.x. [Online]. Available: https://onlinelibrary.wiley.com/doi/abs/10.1111/j.1477-9730.1984.tb00505.x.

[7] J. Paul Siebert and S. J. Marshall, "Human body 3D imaging by speckle texture projection photogrammetry," *Sensor Review*, vol. 20, no. 3, pp. 218–226, 2000. DOI: 10.1108/02602280010372368. [Online]. Available: https://doi.org/10.1108/02602280010372368.

[8] A. Anand, V. K. Chhaniwal, P. Almoro, G. Pedrini, and W. Osten, "Shape and deformation measurements of 3D objects using volume speckle field and phase retrieval," *Opt. Lett.*, vol. 34, no. 10, pp. 1522–1524, May 2009. DOI: 10.1364/OL.34.001522. [Online]. Available: http://ol.osa.org/abstract.cfm?URI=ol-34-10-1522.

[9] M. R. Bennett, D. Huddart, and S. Gonzalez, "Preservation and analysis of three-dimensional footwear evidence in soils: The application of optical laser scanning," in *Criminal and Environmental Soil Forensics*, K. Ritz, L. Dawson, and D. Miller, Eds.

Dordrecht: Springer Netherlands, 2009, pp. 445–461, ISBN: 978-1-4020-9204-6. DOI: 10.1007/978-1-4020-9204-6_28. [Online]. Available: https://doi.org/10.1007/978-1-4020-9204-6_28.

[10] M. Tuceryan, J. Y. Zheng, R. E. Gamage, and A. Joshi, "A high resolution 3D tire and footprint impression acquisition for forensics applications," in *Proceedings of the 2013 IEEE Workshop on Applications of Computer Vision (WACV)*, ser. WACV '13, USA: IEEE Computer Society, 2013, pp. 317–322, ISBN: 9781467350532. DOI: 10.1109/WACV.2013.6475035. [Online]. Available: https://doi.org/10.1109/WACV.2013.6475035.

[11] R. E. Gamage, A. Joshi, J. Y. Zheng, and M. Tuceryan, "A 3D impression acquisition system for forensic applications," in *Advances in Depth Image Analysis and Applications*, X. Jiang, O. R. P. Bellon, D. Goldgof, and T. Oishi, Eds., Berlin, Heidelberg: Springer Berlin Heidelberg, 2013, pp. 9–20, ISBN: 978-3-642-40303-3.

[12] M. Tuceryan and J. Y. Zheng, "Digitizing device to capture track impression," National Institute of Justice, Washington DC, Tech. Rep. 2010-DN-BX-K145 242699, Jun. 2013.

[13] D. A. Komar, S. Davy-Jow, and S. J. Decker, "The use of a 3-D laser scanner to document ephemeral evidence at crime scenes and postmortem examinations," *Journal of Forensic Sciences*, vol. 57, no. 1, pp. 188–191, 2012. DOI: 10.1111/j.1556-4029.2011.01915.x. eprint: https://onlinelibrary.wiley.com/doi/pdf/10.1111/j.1556-4029.2011.01915.x. [Online]. Available: https://onlinelibrary.wiley.com/doi/abs/10.1111/j.1556-4029.2011.01915.x.

[14] R. Siderits, J. Birkenstamm, F. Khani, E. Sadamin, and J. Godyn, "Three-dimensional laser scanning of "crime scene gum" as a forensic method demonstrating the creation of virtual tooth surface contour and web-based rapid model fabrication," Tech. Rep. 2, Apr. 2010.

[15] J. Salvi, S. Fernandez, T. Pribanic, and X. Llado, "A state of the art in structured light patterns for surface profilometry," *Pattern Recognition*, vol. 43, no. 8, pp. 2666–2680, 2010, ISSN: 0031-3203. DOI: https://doi.org/10.1016/j.patcog.2010.03.004. [Online]. Available: http://www.sciencedirect.com/science/article/pii/S003132031000124X.

[16] S. Rusinkiewicz, O. Hall-Holt, and M. Levoy, "Real-time 3D model acquisition," *ACM Trans. Graph.*, vol. 21, no. 3, pp. 438–446, Jul. 2002, ISSN: 0730-0301. DOI: 10.1145/566654.566600. [Online]. Available: https://doi.org/10.1145/566654.566600.

[17] L. Zhang, N. Snavely, B. Curless, and S. M. Seitz, "Spacetime faces: High resolution capture for modeling and animation," *ACM Trans. Graph.*, vol. 23, no. 3, pp. 548–558, Aug. 2004, ISSN: 0730-0301. DOI: 10.1145/1015706.1015759. [Online]. Available: https://doi.org/10.1145/1015706.1015759.

[18] C. Guan, L. G. Hassebrook, and D. L. Lau, "Composite structured light pattern for three-dimensional video," *Opt. Express*, vol. 11, no. 5, pp. 406–417, Mar. 2003. DOI: 10.1364/OE.11.000406. [Online]. Available: http://www.opticsexpress.org/abstract.cfm?URI=oe-11-5-406.

[19] J. Davis, D. Nehab, R. Ramamoorthi, and S. Rusinkiewicz, "Spacetime stereo: A unifying framework for depth from triangulation," *IEEE Transactions on Pattern Analysis and Machine Intelligence*, vol. 27, no. 2, pp. 296–302, 2005. DOI: 10.1109/TPAMI.2005.37.

[20] S. Zhang, "Recent progresses on real-time 3D shape measurement using digital fringe projection techniques," *Optics and Lasers in Engineering*, vol. 48, no. 2, pp. 149–158, 2010, Fringe Projection Techniques, ISSN: 0143-8166. DOI: https://doi.org/10.1016/j.optlaseng.2009.03.008. [Online]. Available: http://www.sciencedirect.com/science/article/pii/S0143816609000529.

[21] S. Zhang, "High-speed 3D imaging with digital fringe projection technique," in, 1st ed. New York, NY: CRC Press, 2016, p. 71, ISBN: 978-1482234336.

[22] M. Takeda, H. Ina, and S. Kobayashi, "Fourier-transform method of fringe-pattern analysis for computer-based topography and interferometry," *J. Opt. Soc. Am.*, vol. 72, no. 1, pp. 156–160, Jan. 1982. DOI: 10.1364/JOSA.72.000156. [Online]. Available: http://www.osapublishing.org/abstract.cfm?URI=josa-72-1-156.

[23] J. C. Wyant, "White light interferometry," in *Holography: A Tribute to Yuri Denisyuk and Emmett Leith*, H. J. Caulfield, Ed., International Society for Optics and Photonics, vol. 4737, SPIE, 2002, pp. 98–107. DOI: 10.1117/12.474947. [Online]. Available: https://doi.org/10.1117/12.474947.

[24] S. Zhang and P. S. Huang, "High-resolution, real-time three-dimensional shape measurement," *Optical Engineering*, vol. 45, no. 12, pp. 1–8, 2006. DOI: 10.1117/1.2402128. [Online]. Available: https://doi.org/10.1117/1.2402128.

[25] S. Zhang, D. Royer, and S.-T. Yau, "GPU-assisted high-resolution, real-time 3-D shape measurement," *Opt. Express*, vol. 14, no. 20, pp. 9120–9129, Oct. 2006. DOI: 10.1364/OE.14.009120. [Online]. Available: http://www.opticsexpress.org/abstract.cfm?URI=oe-14-20-9120.

[26] S. Lei and S. Zhang, "Flexible 3-D shape measurement using projector defocusing," *Opt. Lett.*, vol. 34, no. 20, pp. 3080–3082, Oct. 2009. DOI: 10.1364/OL.34.003080. [Online]. Available: http://ol.osa.org/abstract.cfm?URI=ol-34-20-3080.

[27] S. Zhang, D. Van Der Weide, and J. Oliver, "Superfast phase-shifting method for 3-D shape measurement," *Opt. Express*, vol. 18, no. 9, pp. 9684–9689, Apr. 2010. DOI:

10.1364/OE.18.009684. [Online]. Available: http://www.opticsexpress.org/abstract.cfm?URI=oe-18-9-9684.

[28] S. Naether, U. Buck, W. Bernhard, C. Zingg, and M. J. Thali, "Non-contact documentation of physical characteristics of ecstasy tablets, hemp coins, and imprint punches by using 3D optical surface scanning," *Canadian Society of Forensic Science Journal*, vol. 41, no. 4, pp. 191–198, 2008. DOI: 10.1080/00085030.2008.10757176. eprint: https://doi.org/10.1080/00085030.2008.10757176. [Online]. Available: https://doi.org/10.1080/00085030.2008.10757176.

[29] T. J. U. Thompson and P. Norris, "A new method for the recovery and evidential comparison of footwear impressions using 3D structured light scanning.," *Science & justice : journal of the Forensic Science Society*, vol. 58, no. 3, pp. 237–243, May 2018. DOI: 10.1016/j.scijus.2018.02.001.

[30] *Guide for casting footwear and tire impression evidence*, Mar. 2007. [Online]. Available: http://treadforensics.com/images/swgtread/standards/current/swgtread_11_casting_200703.pdf.

[31] S. Zhang and P. S. Huang, "Novel method for structured light system calibration," *Optical Engineering*, vol. 45, no. 8, pp. 1–8, 2006. DOI: 10.1117/1.2336196. [Online]. Available: https://doi.org/10.1117/1.2336196.

[32] B. Li, N. Karpinsky, and S. Zhang, "Novel calibration method for structured-light system with an out-of-focus projector," *Appl. Opt.*, vol. 53, no. 16, pp. 3415–3426, Jun. 2014. DOI: 10.1364/AO.53.003415. [Online]. Available: http://ao.osa.org/abstract.cfm?URI=ao-53-16-3415.

[33] D. Malacara, *Optical shop testing*, 3rd ed. John Wiley and Sons, 2007.

[34] S. Lei and S. Zhang, "Digital sinusoidal fringe pattern generation: Defocusing binary patterns vs focusing sinusoidal patterns," *Optics and Lasers in Engineering*, vol. 48, no. 5, pp. 561–569, 2010, ISSN: 0143-8166. DOI: https://doi.org/10.1016/j.optlaseng.2009.12.002. [Online]. Available: http://www.sciencedirect.com/science/article/pii/S0143816609002887.

[35] L. Ekstrand and S. Zhang, "Three-dimensional profilometry with nearly focused binary phase-shifting algorithms," *Opt. Lett.*, vol. 36, no. 23, pp. 4518–4520, Dec. 2011. DOI: 10.1364/OL.36.004518. [Online]. Available: http://ol.osa.org/abstract.cfm?URI=ol-36-23-4518.

[36] L. Ekstrand and S. Zhang, "Autoexposure for three-dimensional shape measurement using a digital-light-processing projector," *Optical Engineering*, vol. 50, no. 12, pp. 1–8, 2011. DOI: 10.1117/1.3662387. [Online]. Available: https://doi.org/10.1117/1.3662387.

[37] S. Zhang, "Rapid and automatic optimal exposure control for digital fringe projection technique," *Optics and Lasers in Engineering*, vol. 128, p. 106 029, 2020, ISSN: 0143-8166. DOI: https://doi.org/10.1016/j.optlaseng.2020.106029. [Online]. Available: http://www.sciencedirect.com/science/article/pii/S0143816619318299.